

ARTICLE

# Cell cortex regulation by the planar cell polarity protein Prickle1

Yunyun Huang<sup>1</sup> and Rudolf Winklbauer<sup>1</sup>

The planar cell polarity pathway regulates cell polarity, adhesion, and rearrangement. Its cytoplasmic core components Prickle (Pk) and Dishevelled (Dvl) often localize as dense puncta at cell membranes to form antagonizing complexes and establish cell asymmetry. In vertebrates, Pk and Dvl have been implicated in actomyosin cortex regulation, but the mechanism of how these proteins control cell mechanics is unclear. Here we demonstrate that in *Xenopus* prechordal mesoderm cells, diffusely distributed, cytoplasmic Pk1 up-regulates the F-actin content of the cortex. This counteracts cortex down-regulation by Dvl2. Both factors act upstream of casein kinase II to increase or decrease cortical tension. Thus, cortex modulation by Pk1 and Dvl2 is translated into mechanical force and affects cell migration and rearrangement during radial intercalation in the prechordal mesoderm. Pk1 also forms puncta and plaques, which are associated with localized depletion of cortical F-actin, suggesting opposite roles for diffuse and punctate Pk1.

## Introduction

Planar cell polarity (PCP) proteins were initially identified as members of two protein complexes whose mutually exclusive, asymmetric localization at the apical cell periphery determines polarity in the plane of *Drosophila* epithelial tissue. Core PCP genes encode the transmembrane proteins Frizzled (Fz), Strabismus (Stbm)/van Gogh-like (Vangl), and Flamingo (Fmi)/Celsr, and the cytoplasmic factors Dishevelled (Dvl) and Prickle (Pk), and recruitment of the cytoplasmic components to the cell membrane and their interaction with the transmembrane proteins to form dense puncta is considered a hallmark of PCP signaling (Adler, 2002; Strutt, 2003; Gray et al., 2011; Wallingford, 2012; Strutt et al., 2011, 2016).

In the vertebrate gastrula, PCP genes are involved in the control of cell polarity, adhesion, and motility. Initially, the Fz-Dvl branch of PCP signaling had been shown to regulate convergent extension in zebrafish and *Xenopus laevis* (Heisenberg et al., 2000; Tada and Smith, 2000; Wallingford et al., 2000). With the involvement of Wnt ligands upstream of Fz and the central role of Dvl in Wnt signaling, the PCP module diversified rapidly into several noncanonical Wnt pathways. Activation of RhoA, Rac, JNK, Daam, or Ca<sup>2+</sup> signaling linked these pathways to the regulation of the cytoskeleton and to transcription control (Tada and Kai, 2009; Kestler and Kuhl, 2008; van Amerongen and Nusse, 2009; Lapebie et al., 2011). Moreover, the multi-functional Dvl proteins interact with numerous diverse factors, for example ephrinB1, glypican-4, or syndecan-4 (Wallingford

and Habas, 2005; Gao and Chen, 2010), further corroding the concept of a defined vertebrate PCP pathway (Kestler and Kuhl, 2008) and suggesting PCP-independent functions of core PCP components. The Stbm/Vangl-Pk branch of PCP signaling is likewise required for convergent extension in zebrafish and *Xenopus* (Jessen et al., 2002; Darken et al., 2002; Carreira-Barbosa et al., 2003; Veeman et al., 2003; Takeuchi et al., 2003; Shindo et al., 2019).

In *Drosophila* epithelia as well as in vertebrate embryonic cells, diffuse cytoplasmic Pk and Dvl proteins coexist with the punctate form of these factors. In *Xenopus* chordamesoderm engaged in convergent extension, diffuse Dvl2 is slightly polarized along the mediolateral axis of cells, whereas small Dvl2 puncta are randomly distributed (Kinoshita et al., 2003; Panousopoulou et al., 2013). In the zebrafish, by contrast, Dvl puncta are enriched at the posterior side of converging dorsal mesoderm cells (Yin et al., 2008). Pk1 forms random puncta and large plaques in *Xenopus* chordamesoderm (Daulat et al., 2012). Pk2 puncta in *Xenopus* (Shindo et al., 2019) and Pk1 puncta in zebrafish (Yin et al., 2008) occupy the anterior edges of dorsal mesoderm cells, and Pk also shows a punctate anterior localization in the neural plate of both species (Ciruna et al., 2006; Butler and Wallingford, 2018). Overall, these localization preferences are suggestive of a cell-polarizing function of PCP puncta in vertebrate gastrula tissues.

<sup>1</sup>Department of Cell and Systems Biology, University of Toronto, Toronto, Ontario, Canada.

Correspondence to Rudolf Winklbauer: [r.winklbauer@utoronto.ca](mailto:r.winklbauer@utoronto.ca).

© 2022 Huang and Winklbauer. This article is distributed under the terms of an Attribution–Noncommercial–Share Alike–No Mirror Sites license for the first six months after the publication date (see <http://www.rupress.org/terms/>). After six months it is available under a Creative Commons License (Attribution–Noncommercial–Share Alike 4.0 International license, as described at <https://creativecommons.org/licenses/by-nc-sa/4.0/>).

The commonly held view that Pk and Dvl are activated by membrane recruitment, and the rather uniform distribution of their diffuse forms, could suggest a mere supportive role of diffuse Pk and Dvl as reservoirs for puncta formation. Here we examine the role of diffuse Pk1 in prechordal mesoderm (PCM) cells of the *Xenopus* gastrula. We propose that Pk1 functions as part of a regulatory module in which diffuse Pk1 activates and Dvl2 inhibits casein kinase II (CKII) activity, which in turn controls the F-actin content of the cell cortex. Surprisingly, while diffuse Pk1 promotes F-actin formation, Pk1 puncta are correlated with diminished cortex density, suggesting opposite roles for diffuse and punctate Pk1.

By acting on the cell cortex, Pk1 affects a main interaction hub that connects signaling pathways to motile cell behaviors. The cortex consists of a submembrane meshwork of branched and bundled actin filaments; filament nucleators like the Arp2/3 complex and formins; regulators of filament assembly and disassembly; filament cross-linkers; and actin-membrane linkers (Biro et al., 2013; Chugh and Paluch, 2018). Nonmuscle myosin II renders the cortex contractile (Pasternak et al., 1989; Zaidel-Bar et al., 2015; Chugh and Paluch, 2018) and generates a sustained cortical tension that tends to round up isolated cells (Evans and Yeung, 1989; Salbreux et al., 2012; Clark et al., 2013). Cortex contractility is essential for cell migration, for example by pushing the cell body forward by rear-end contractions, pulling it after an advancing protrusion, or generating cortical flow (Huang and Winklbauer, 2018).

While instrumental in cell locomotion, cortical tension with its tendency to generate round cell shapes must be overcome during adhesion, when cells flatten against each other. The release of binding energy by interacting adhesion molecules such as cadherins is usually not sufficient for this effect, and close attachment of cells requires the downregulation of cortical tension at cell–cell interfaces. The adhesion strength determined in this way can be measured as tissue surface tension (Brodlund and Chen, 2000; Amack and Manning, 2012; Winklbauer, 2015). Thus, with the cell cortex, diffuse Pk1 affects at the same time two basic features that have been implicated as targets of vertebrate PCP signaling: cell motility and cell–cell adhesion.

## Results

### Pk1 function is necessary for PCM cell migration and rearrangement

In the gastrula, PDGF-A from the ectodermal blastocoel roof (BCR) attracts PCM cells to directionally migrate between and over each other toward the BCR, thus intercalating and eventually accumulating at the PCM–BCR boundary. When a PCM and a BCR explant are placed in contact, intercalation by PCM cell-on-cell migration occurs in vitro (Fig. 1 A; Damm and Winklbauer, 2011). In untreated explants, laterally adjacent cells move apart, and cells move over each other. By repeatedly shrinking and breaking existing contacts, and establishing and expanding new contacts, cells in an initially coherent cluster become dispersed (Fig. 1 A and Video 1). Knockdown of Pk1 with a previously characterized morpholino oligonucleotide (Takeuchi et al., 2003) perturbed cell rearrangement, and cells

less often exchanged neighbors (Fig. 1, A and A'; and Video 2). Nevertheless, the strongly elongating cells (Fig. 1 B) were still biased toward the BCR, although less precisely (Fig. 1 C).

Knockdown of Pk1 attenuated cell velocity (Fig. 1, D–G). Net translocation and persistence were reduced by half (Fig. 1, F and G). When intercalating, cells migrate on each other's surface at comparable speed. As the velocity of a given cell is added to that of the substrate cell ahead of it, which in turn is added to that of a cell further ahead, a velocity gradient forms (Damm and Winklbauer, 2011; Huang and Winklbauer, 2018) as seen in control explants (Fig. 1 E). Morphant cells retained some motility, but with intercalation, the velocity gradient was diminished (Fig. 1 E). Overall, Pk1 is required for radial intercalation in PCM, and its knockdown affects migration velocity, cell shape, and rearrangement. However, it disturbs cell orientation only moderately. Conversely, rapid, persistent cell migration was retained upon Dvl2 knockdown, but cells reoriented and moved in parallel to the tissue boundary (Fig. 1 D). At the embryo level, gastrulation is arrested by Pk1 knockdown and rescued by Pk1 mRNA coinjection (Fig. S1 A). The arrest phenotype suggests that processes beyond PCM radial intercalation are affected, such as the tissue-autonomous mesoderm involution seen in lip explants (Fig. S1 B; Evren et al., 2014).

### Pk1 protein occurs in diffuse and in punctate form in the PCM

Pk forms puncta or plaques at cell membranes, and membrane recruitment is often taken to indicate Pk activity. However, Pk occurs in addition to puncta also in diffuse form, as seen by immunofluorescence (Fig. S2). Expressing low amounts of fluorescently tagged Pk1-venus also visualizes Pk1 localization (Veeman et al., 2003; Daulat et al., 2012). In PCM explants, diffuse Pk1-venus fills the cytoplasm of the cell body between yolk platelets and appears enriched near the cell surface (Fig. 2, A and B). Within this peripheral zone of diffuse Pk1, puncta and plaques composed of small puncta are scattered (Fig. 2, A and B). In line plots, puncta are four times more intense than diffuse regions, and the intensity of diffuse Pk1 in the cell interior is half that at the membrane (Fig. 2 C).

In variably sized fragments of PCM, homogeneously distributed diffuse Pk1 is always present (Fig. 2, D–G and I–L) and similarly intense (Fig. 2, H and M). However, large Pk1 plaques diminish with decreasing fragment size, to be replaced by small puncta (Fig. 2, D–G, I–L, and N), and average puncta intensity is reduced (Fig. 2, H and M). Unlike puncta size, the number of puncta or plaques per cell does not significantly differ with fragment size, but it decreases abruptly in single cells (Fig. 2 O).

In such isolated, nonadherent PCM cells, Pk1 puncta are negligible (Fig. 2 O). Diffuse Pk1 occupies a  $1.7 \pm 0.4$ - $\mu\text{m}$ -wide zone below the cell membrane (Fig. 3, A and C). The same zone stains intensely for F-actin, marking the cell cortex (Fig. 3, B and C). On rare occasions, small Pk1 puncta appear at the membrane side of the cortex (Fig. 3 B). Diffuse Pk1 does not strictly colocalize with the cortical F-actin. When the latter was perturbed using the formin inhibitor, SMIFH2, the cortex became wider and the zone of diffuse Pk1 widened in parallel (Fig. 3, B and C). Importantly, when the F-actin cortex occasionally separated into an outer and an inner layer, Pk1 localization remained

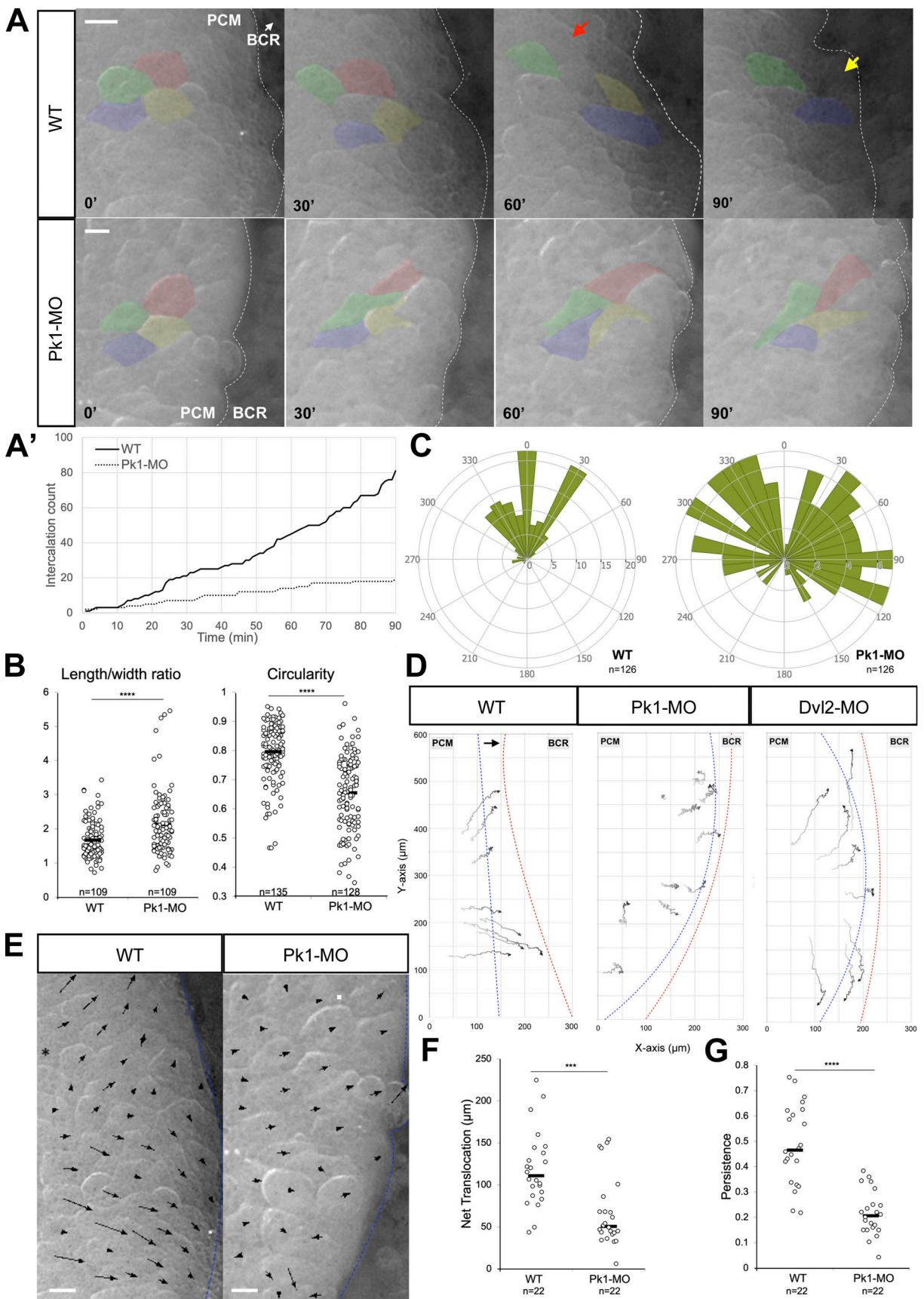


Figure 1. **PK1 knockdown disrupts cell rearrangement in the PCM.** (A) WT and Pk1-MO cells in PCM explants in contact with BCR (dashed lines, PCM-BCR boundary). Red and yellow arrows indicate migration of unlabeled cell over red and yellow cells, respectively. Time in minutes. Scale bars, 20  $\mu\text{m}$ .

**(A)** Quantification of cell intercalation events summed over time in PCM explants. **(B)** Cell length/width ratio (WT,  $n = 109$ ; Pk1-MO,  $n = 109$ ) and circularity (WT,  $n = 135$ ; Pk1-MO,  $n = 128$ ). Bars indicate the mean in all figures. \*\*\*\*,  $P \leq 0.0001$  in a two-tailed Student's  $t$  test. Data distribution was assumed to be normal but was not formally tested. **(C)** Cell orientation in WT ( $n = 126$ ) and Pk1-MO PCM ( $n = 126$ ).  $0^\circ$  indicates orientation toward BCR. **(D)** Tracks of individual cells in WT, Pk1-MO, and Dvl2-MO PCM-BCR explants. Blue and red dashed lines, initial and final tissue boundaries. **(E)** From Videos 1 and 2. Velocity gradient in WT and Pk1-MO PCM. BCR on the right; dashed lines indicate initial tissue boundaries. Scale bars,  $20 \mu\text{m}$ . **(F)** Net translocation of WT ( $n = 22$ ) and Pk1-MO ( $n = 22$ ) cells in explants over 90 min. \*\*\*,  $P \leq 0.001$  in a two-tailed Student's  $t$  test. Data distribution was assumed to be normal but was not formally tested. **(G)** Migration persistence (WT,  $n = 22$ ; Pk1-MO,  $n = 22$ ). \*\*\*\*,  $P \leq 0.0001$  in a two-tailed Student's  $t$  test. Data distribution was assumed to be normal but was not formally tested.

homogeneous and did not match spatial F-actin density variations (Fig. 3, B and B'), inconsistent with direct or indirect stoichiometric binding of Pk1 to F-actin. Instead, both components appear to overlap at the cell periphery. Lack of close Pk1-F-actin association is also seen in cells treated with the Arp2/3 inhibitor CK666 (Fig. 3, B and B'). The dense cortex is dissolved, and only F-actin puncta and commas remain. They are slightly enriched at the periphery but occur also in the cell body between yolk platelets. Pk1 is also weakly enriched near the cell surface, but strongly accumulating in F-actin-free membrane blebs, which are frequent in the treated cells.

#### Diffuse Pk1 and Dvl2 control cortical F-actin levels

That isolated PCM cells lack puncta offers an opportunity to study the function of diffuse Pk1, whose overlap with the cell cortex raises the possibility that it regulates cortical F-actin. Indeed, knockdown of Pk1 reduced staining with fluorescent phalloidin by half, and coinjection of Pk1-venus mRNA reversed this effect (Fig. 4, A–C). Overexpression of Pk1 increased cortex density by more than threefold (Fig. 4, A and F). Together, these data are consistent with an upregulation of cortical F-actin levels by diffuse Pk1. Dvl2 has an opposite effect. Knockdown increased F-actin levels in a dose-dependent fashion by  $\leq 2.5$ -fold (Fig. 4, A and D). Moreover, a full rescue of cortex density after Pk1 knockdown was attained at a medium Dvl2-MO concentration (Fig. 4, A and E). Apparently, a balance between Pk1 and Dvl2 activities is required for a normal level of F-actin at the PCM cortex. With respective effects of Pk1 knockdown in one cell and Dvl2 depletion in another, a maximum difference in cortical F-actin content between the cells of approximately fivefold can be generated. For comparison, *Xenopus* ectoderm cells downregulate the cortex fivefold upon mutual contact to achieve full cell–cell adhesion (David et al., 2014), indicating that the amplitude of Pk1-Dvl2-mediated cortex regulation is in a biologically significant range.

A candidate effector of both Pk1 and Dvl2 is CKII, a ubiquitously expressed serine/threonine kinase that associates with Dvl (Willert et al., 1997; Gao and Wang, 2006) and Pk (Daulat et al., 2012) and regulates actin dynamics (Canton et al., 2005; Xavier et al., 2012) and cell contractility and motility (Kramerov et al., 2012). The CKII inhibitor 4,5,6,7-tetrabromobenzotriazole (TBB) reduced F-actin directly after application and to a similar extent as Pk1 knockdown (Fig. 4, A and E). In Pk1-depleted cells, inhibition of CKII did not cause further reduction (Fig. 4, A and E). In Dvl2 morphant or Pk1-overexpressing cells, it reduced F-actin to the same basal level (Fig. 4, A, E, and F). The data are consistent with CKII acting downstream of both Pk1 and Dvl2, suggesting a Pk1-Dvl2-CKII cortex-regulating module. In none of

the loss-of-function experiments was F-actin density reduced by more than half (Fig. 4, C–F), pointing to a Pk1-Dvl2-CKII-independent component of the cortex.

#### Ubiquitous diffuse Pk1 controls F-actin cortex assembly at the cell membrane

PCM cells occasionally form transient, asymmetric membrane blebs. Such blebs develop at a time scale of minutes and propagate wavelike around a cell (Fackler and Grosse, 2008; Fig. 5 A). We used these to examine how the control of the cortex by Pk1-Dvl2-CKII is spatially and temporally organized. A bleb propagates as the membrane, together with a thin layer of cortex, separates from the bulk of the existing cortex at its front. At the detached membrane, the cortex rebuilds to full strength while the remnant of the original cortex, which forms an arc-shaped structure in the cytoplasm, fades and disappears. Transiently, F-actin is thus present in two layers, at the cell membrane and at the yolk-filled cell body (Fig. 5, A and A'). In time-lapse recordings, an initial overshooting of F-actin deposition at the bleb membrane (Clark et al., 2013) and a return to normal levels upon bleb retraction can be observed (Fig. 5 B and Video 3).

In TBB-treated blebs, F-actin is absent from the membrane but present at the surface of the cell body. This layer is continuous with the remaining cortex and equally dense, yet uneven, as if not contractile and not compressing the cell core (Fig. 5, A' and A''). In time-lapse recordings, newly deposited F-actin vanishes from the bleb membrane within a minute of TBB addition (Fig. 5 B' and Video 4). Apparently, normal assembly of new cortex at the detached membrane is inhibited. However, F-actin strands form within the bleb, move toward the surface of the cell body from which the preexisting cortex has disappeared, and accumulate there (Fig. 5 B'), consistent with the formation of a baseline cortex that resists Pk1-Dvl2-CKII inhibition (see Fig. 4). This new cortex structure does not appear to be under tension initially, and in contrast to the remnants of the original cortex at the bleb, it does not dissolve rapidly on the cell body surface (Fig. 5 B'). Together, the bleb data suggest that the F-actin cortex may be attached not only to the cell membrane, but independently also to the cell body. Here, the curved layer of preexisting cortex, detached from the membrane, conforms closely to the surface of a compact ER domain that is restricted to the cell body and does not extend into blebs (Fig. 5 C). Such attachment should prevent the contraction and shriveling of free, contractile actomyosin cortex segments.

Although Pk1-sensitive cortical F-actin assembly occurs at the cell membrane, diffuse Pk1 is homogeneously distributed between cell membrane and ER domain surface and occurs also within the ER domain (Fig. 5 D). Its average density must be

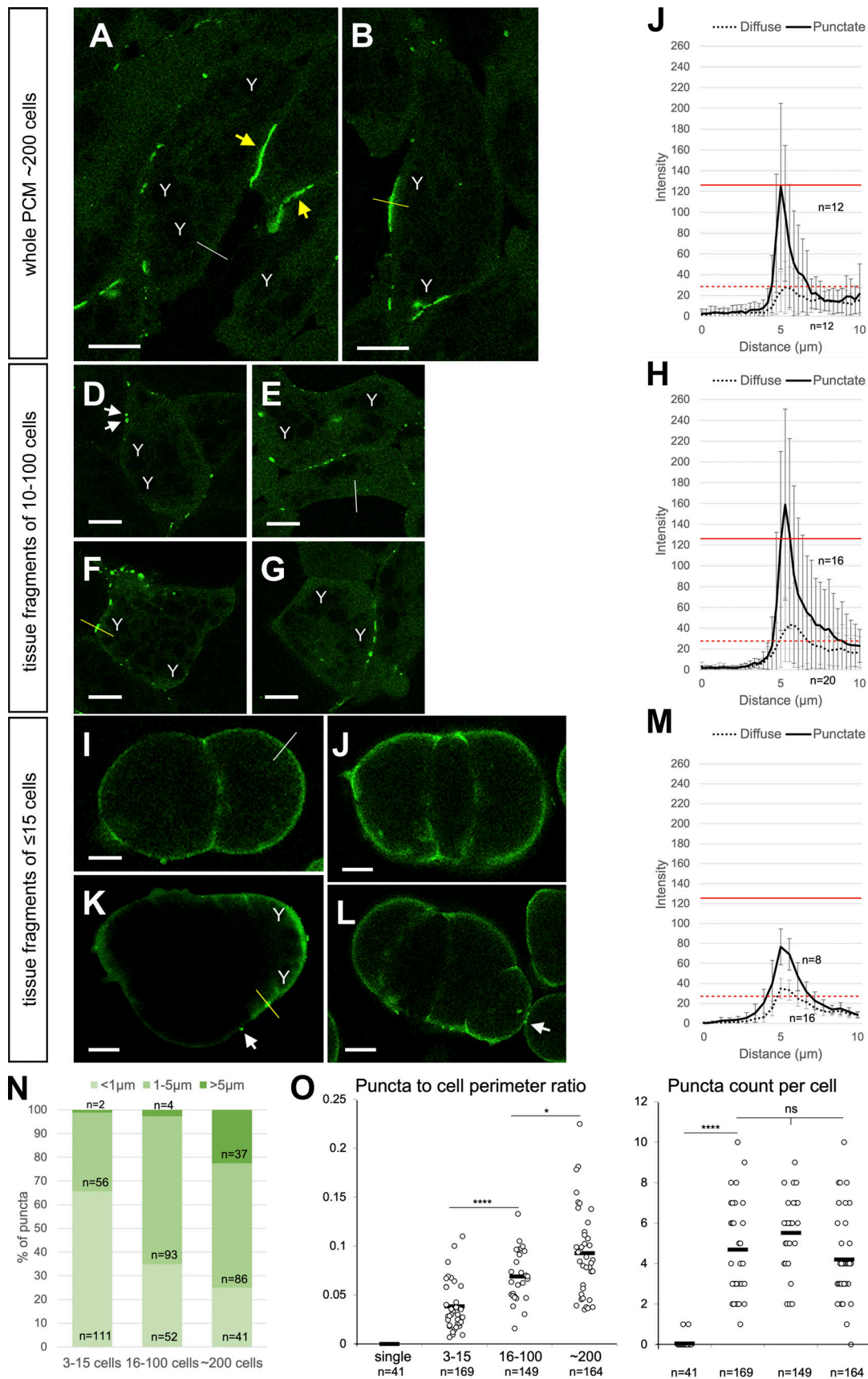


Figure 2. Diffuse and punctate Pk1 in the PCM. (A, B, D-G, and I-L) Whole PCM explants (A and B) and medium sized (D-G) and small (I-L) PCM fragments expressing Pk1-venus. Yellow arrows, Pk1 plaques; white arrows, puncta; Y, yolk platelets; yellow and white lines, positions of line plots at boundaries between

Pk1-venus-labeled and unlabeled cells. Scale bars, 10  $\mu\text{m}$ . **(C, H, and M)** Average intensities of line plots of punctate (solid) and diffuse (dotted) Pk1 from outside (left) to inside (right) of cells. Means  $\pm$  SD are shown. Solid and dashed red lines indicate peak values of punctate and diffuse Pk1 in whole PCM explants. Error bars indicate SD. Whole PCM explants: punctate,  $n = 12$ ; diffuse,  $n = 12$ . Medium-sized fragments: punctate,  $n = 16$ ; diffuse,  $n = 20$ . Small fragments: punctate,  $n = 8$ ; diffuse,  $n = 16$ .  $n$ , number of cells. **(N)** Fraction of small ( $<1 \mu\text{m}$ ;  $n = 2$  in small PCM fragments,  $n = 4$  in medium-sized fragments,  $n = 37$  in whole explants) and medium-sized ( $1\text{--}5 \mu\text{m}$ ;  $n = 56$  in small fragments,  $n = 93$  in medium-sized fragments,  $n = 86$  in whole explants) puncta and large plaques ( $>5 \mu\text{m}$ ;  $n = 111$  in small fragments,  $n = 52$  in medium-sized fragments,  $n = 41$  in whole explants) measured along cell membranes in PCM fragments. Counts of puncta-stained cells were pooled from experiment replicates to calculate fractions.  $n$ , number of puncta. **(O)** Ratio of total puncta length to cell perimeter and average number of puncta per cell in isolated cells and different-sized fragments as in N. For both measurements,  $n = 41$  for single cells,  $n = 169$  for small PCM fragments,  $n = 149$  for medium-sized fragments,  $n = 164$  for whole explants.  $n$ , number of cells. Bars indicate the mean. \*,  $P \leq 0.05$ ; \*\*\*,  $P \leq 0.0001$  in a two-tailed Student's  $t$  test. Data distribution was assumed to be normal but was not formally tested.

reduced in the cell body by being excluded from yolk platelets and ER lumen. The distribution of inert fluorescent dextran, which is not expected to be actively enriched at the cortex, closely resembles that of diffuse Pk1 (Fig. 5, E, E', F, and F'), suggesting that, like dextran, Pk1 is freely dispersing in the cytoplasm and appears enriched in the cortex zone only because of the absence of space-filling subcellular structures. An ER-free, Pk1-filled cortical zone and lower apparent Pk1 intensity in the cell core also characterize tissues (Fig. S3). The thickness of ER-free space and Pk1 layer are identical, and both are narrower at Pk1 puncta and wider in diffuse sections (Fig. S3). We propose that Pk1, and probably Dvl2 as well (Panousopoulou et al., 2013), are evenly distributed in the cytoplasm but appear sparse in the cell core, where they are diluted by yolk platelets and ER.

#### Pk1-Dvl2-CKII-regulated cortex density modulates cortical tension

In *Xenopus* gastrula ectoderm cells, cortical F-actin density is related to the strength of cortical tension (David et al., 2014). To link cortex regulation by Pk1 to cell mechanics, cortical tensions of WT and Pk1-depleted cells were compared. In a pair of identical cells, cortical tension  $\beta$  at the free cell surfaces and the reduced tension  $\beta^*$  at the cell-cell contact balance each other and determine the contact angle  $2\theta$  (Winklbauer, 2015; Fig. 6 D) according to

$$\cos\theta = \beta^* / \beta. \quad (1)$$

With the same cortical tensions in both cells, the same Laplace pressure is generated in each, and the cell-cell interface is straight. When tensions in cells A and B differ, the more contractile cell generates higher pressure and bulges into the lower-tension cell, and the interface is curved. The ratio of their respective cortical tensions,  $\beta_A$  and  $\beta_B$ , can be calculated from contact angle contributions  $\theta_A$  and  $\theta_B$  (Canty et al., 2017; Kashkooli et al., 2021; Fig. 6 A). Balancing tensions at the free surfaces of the cells,  $\beta_A$  and  $\beta_B$ , and at the interface,  $\beta_{AB}^*$ , requires (Fig. 6 A)

$$\beta_A \sin\theta_A = \beta_B \sin\theta_B, \quad (2)$$

and

$$\beta_A \cos\theta_A + \beta_B \cos\theta_B = \beta_{AB}^*. \quad (3)$$

Eq. 2 is sufficient to calculate the ratio  $\beta_B/\beta_A$  from the contact angles,  $\beta_B/\beta_A = \sin\theta_A/\sin\theta_B$ .

Homotypic pairs of WT or of Pk1-depleted cells maintain on average straight cell-cell contacts as expected, and the ratio of cortex tensions is 1.007 and 1.002, respectively (Fig. 6, B and C). If cortical tension is higher in WT cells and lower in Pk1-depleted morphant cells, the contact interface should bulge into the morphant cell in heterotypic pairs. This is indeed observed (Fig. 6 B), and according to Eq. 2,  $\beta_{PkMO}/\beta_{WT} = \sin\theta_{WT}/\sin\theta_{PkMO} = 0.530$ . Thus, Pk1 knockdown reduced cortical tension by half (Fig. 6 C), in close agreement with the reduced cortical F-actin content after Pk1 depletion (see Fig. 4 C).

To estimate absolute values of cortical tensions, tissue surface tension  $\sigma$  can be measured in explants (David et al., 2014).  $\sigma$  corresponds to the difference between cortical tension  $\beta$  at the free explant surface and the reduced tension  $\beta^*$  at cell-cell contacts (Winklbauer, 2015; Fig. 6 D):

$$\sigma = \beta - \beta^*. \quad (4)$$

As in cell pairs, the ratio of the two tensions is related to contact angle  $2\theta$  at the explant surface by Eq. 1, and eliminating  $\beta^*$  from Eqs. 1 and 4 gives  $\beta = \sigma/(1 - \cos\theta)$  (Winklbauer, 2015; Fig. 6 D). From tissue surface tensions measured by Axisymmetric Drop Shape Analysis (ADSA; R o and Neumann, 1997; Luu et al., 2011) and contact angle data (Fig. 6, E and F), a cortical tension  $\beta$  of  $0.33 \pm 0.19 \text{ mJ/m}^2$  was calculated for untreated PCM, similar to the previously reported value (David et al., 2014). When cells were depleted of Pk1, Dvl2, or both,  $\beta$  was decreased 0.5-fold, increased 1.5-fold, or left unchanged, respectively, paralleling the changes in cortical F-actin content determined above (Fig. 6 G). Apparently, the effects of Pk1-Dvl2-CKII on F-actin are translated into respective cortical tension differences. Notably, F-actin density measured in single cells in the absence of Pk1 puncta predicts cortical tension changes in puncta-less cell pairs, but also in puncta-rich large explants, suggesting that diffuse Pk1 controls cortical tension under both conditions.

#### Pk1 controls rear-end retraction and cell separation

To see whether Pk1 puncta play a role in PCM cells, we examined the rear-end retraction during cell-on-cell migration. This process involves a gradual shrinking of the contact area between two PCM cells and eventual cell separation, which is impaired in Pk1 morphants. Instead of remaining straight or gently curved, the trailing edge of cells narrows and elongates excessively to form actin-filled retraction fibers (Fig. 7 A). Their F-actin core eventually snaps and curls up as it recoils, leaving an empty

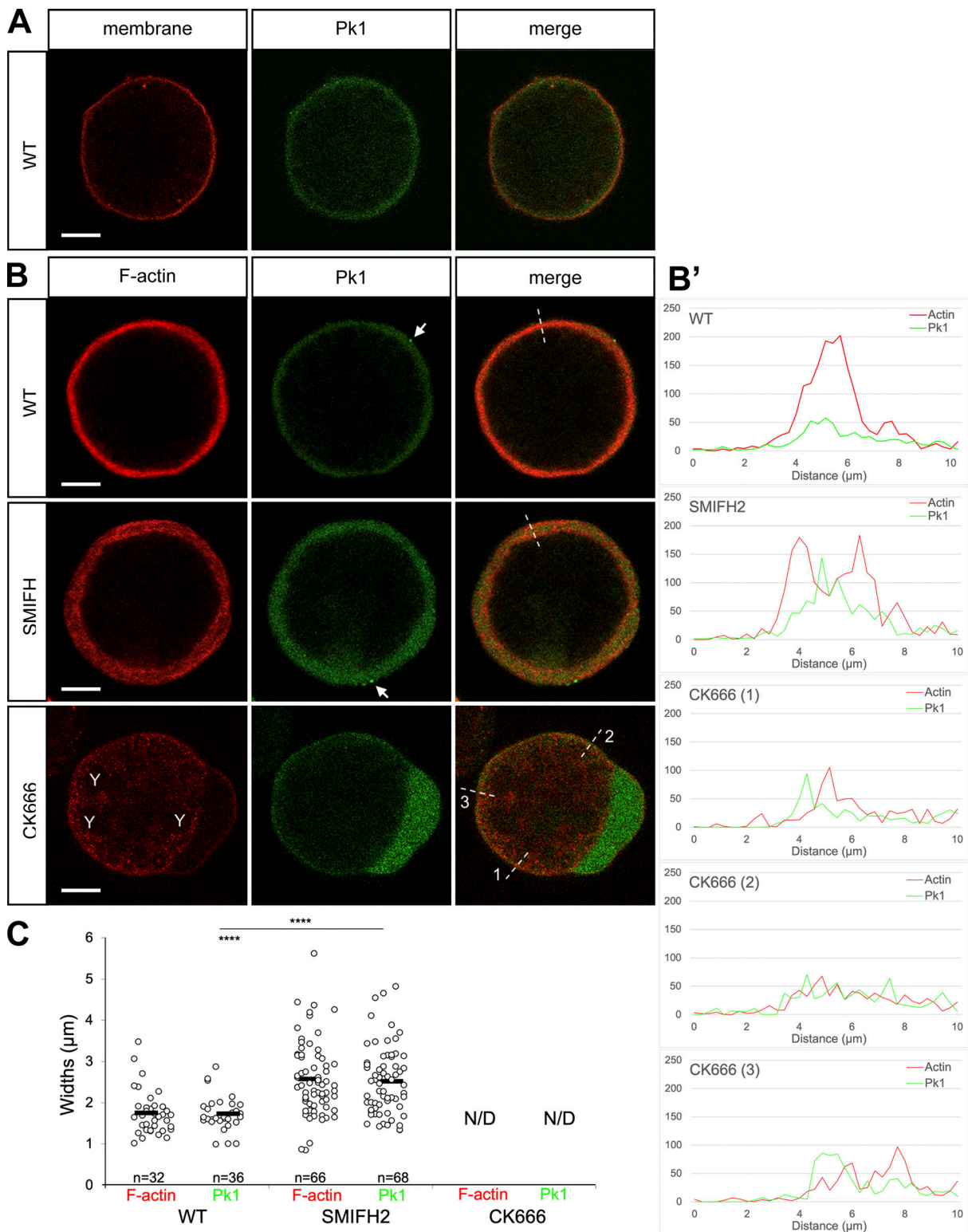


Figure 3. **Diffuse Pk1 overlaps with cortical F-actin.** (A) PCM cell labeled with mb-RFP and Pk1-venus. Scale bar, 10 μm. (B) WT and SMIFH2- and CK666-treated PCM cells labeled with LifeAct-Ruby and Pk1-venus. Arrows, small Pk1 puncta. Y, yolk platelets. Scale bars, 10 μm. (B') Line plots of LifeAct-Ruby and Pk1-venus intensities at dotted lines in B. (C) Widths of F-actin (LifeAct-Ruby) and diffuse Pk1-venus zones in WT (F-actin,  $n = 32$ ; Pk1,  $n = 36$ ) and SMIFH2-treated (F-actin,  $n = 66$ ; Pk1,  $n = 68$ ) cells. F-actin and Pk1-venus became dispersed in CK666-treated cells, and the widths could not be determined (N/D).  $n$ , number of cells. Means  $\pm$  SD are shown. \*\*\*\*,  $P < 0.0001$  in a two-tailed Student's  $t$  test. Data distribution was assumed to be normal but was not formally tested.

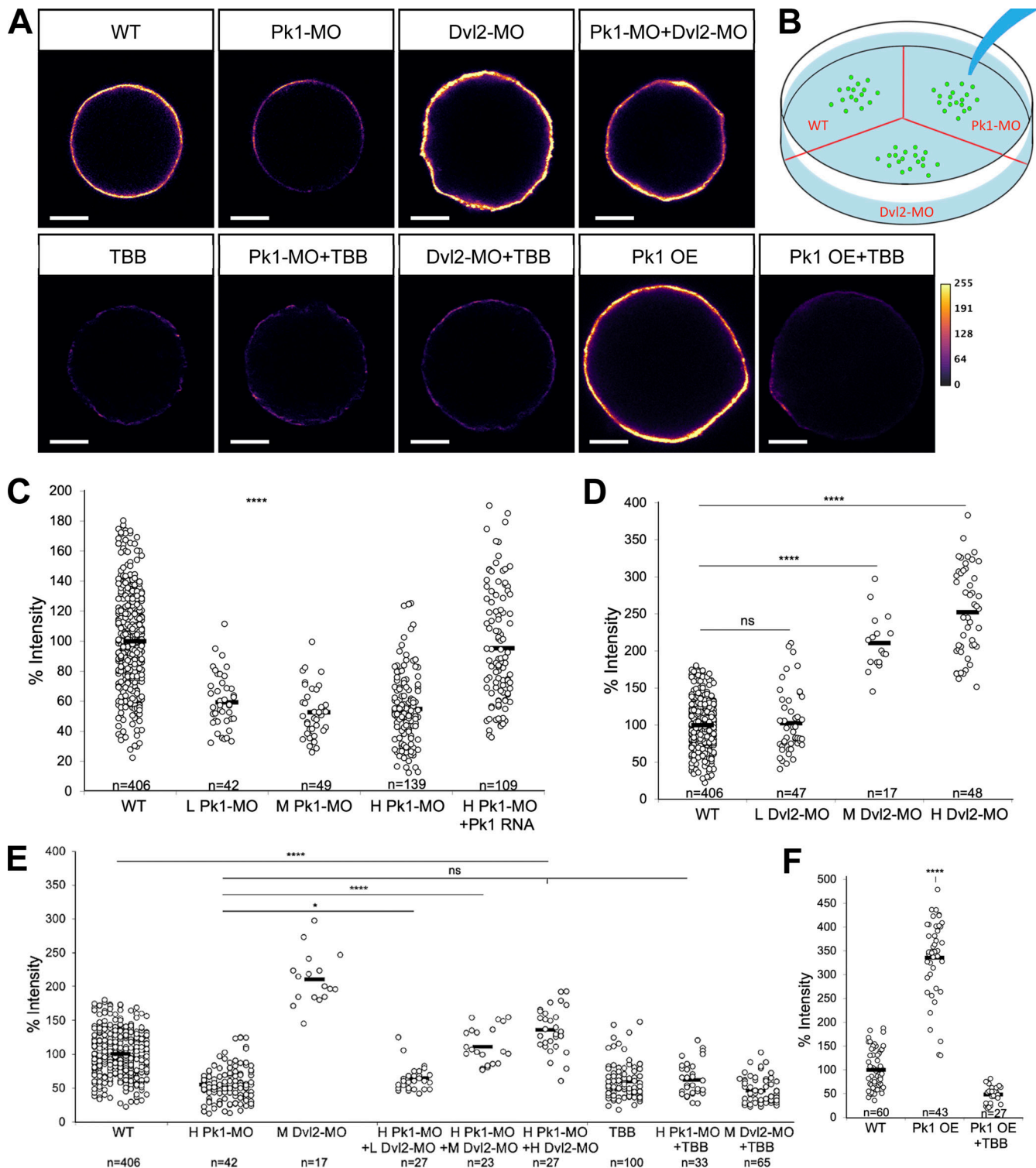


Figure 4. **Diffuse Pk1 and Dvl2 control cortical F-actin levels.** (A) Single PCM cells stained with phalloidin Alexa Fluor 488, pseudo-colored using MPL-Inferno to show intensity spectrum. Pk1-MO 40 ng/bl; Dvl2-MO 24 ng/bl; TBB 10  $\mu$ M; Pk1-OE 500 pg/bl. Scale bars, 10  $\mu$ m. (B) Differently treated cells were stained simultaneously in a single dish to minimize unspecific intensity differences. (C-F) Cortical F-actin intensity in phalloidin-stained cells. Average intensity was calculated from pooled measurements of WT cells, and treated cells were all normalized to this average to give the percentage intensity. *n*, number of cells. (C) Relative staining intensity of cells with low (L, 13 ng/bl, *n* = 42), medium (M, 27 ng/bl, *n* = 49), and high (H, 40 ng/bl, *n* = 139) doses of Pk1-MO and rescue with Pk1-venus-RNA (500 pg/bl) in high Pk1-MO background (*n* = 109). WT, *n* = 406. \*\*\*\*, *P*  $\leq$  0.0001 in a two-tailed Student's *t* test. Data distribution was assumed to be normal but was not formally tested. (D) Relative staining intensity of Dvl2 knockdown cells with low (L, 12 ng/bl, *n* = 47), medium (M, 24 ng/bl, *n* = 17), and high (H, 36 ng/bl, *n* = 48) doses of Dvl2-MO. \*\*\*\*, *P*  $\leq$  0.0001 in a two-tailed Student's *t* test. Data distribution was assumed to be normal but was not formally tested. (E) Relative cortex intensity of Pk1 and Dvl2 double-knockdown cells with combinations of low (L), medium (M), and high (H) morpholino (ns, not significant). (F) Relative cortex intensity of Pk1 OE and Pk1 OE + TBB. \*\*\*\*, *P*  $\leq$  0.0001 in a two-tailed Student's *t* test. Data distribution was assumed to be normal but was not formally tested.

doses, and of cells treated with TBB (10  $\mu$ M) in a WT, Pk1-MO, or Dvl2-MO background. H Pk1-MO and M Dvl2-MO from C and D are included for comparison. H Pk1-MO + L Dvl2-MO,  $n = 27$ ; H Pk1-MO + M Dvl2-MO,  $n = 23$ ; H Pk1-MO + H Dvl2-MO,  $n = 27$ ; TBB,  $n = 100$ ; H Pk1-MO + TBB,  $n = 33$ ; M Dvl2-MO + TBB,  $n = 65$ . \*,  $P \leq 0.05$ ; \*\*\*,  $P \leq 0.001$ ; \*\*\*\*,  $P \leq 0.0001$  in a two-tailed Student's  $t$  test. Data distribution was assumed to be normal but was not formally tested. **(F)** Relative cortex intensity of Pk1 overexpressing (Pk1-OE 500 pg/bl,  $n = 43$ ) and TBB (10  $\mu$ M)-treated Pk1-OE cells ( $n = 27$ ). WT,  $n = 60$ . \*\*\*\*,  $P \leq 0.0001$  in a two-tailed Student's  $t$  test. Data distribution was assumed to be normal but was not formally tested.

membrane tube behind (Video 5). These membrane tethers accumulate at cell surfaces in morphant explants (Fig. 7 B).

Defective tail retraction could be due entirely to reduced cortical tension upon depletion of diffuse Pk1. However, in migrating PCM cells, Pk1 puncta and plaques are enriched in the trailing half (Fig. 8, A and B), hinting at a possible contribution of punctate Pk1. As adhesive contacts between two cells shorten and eventually vanish, Pk1 puncta form, travel along the membrane, join others to form large plaques, or diminish and disappear (Fig. 8, C-E; and Video 6). Puncta dynamics shows a close quantitative association with cell separation (Fig. 8, J and K). Puncta move at a rate of  $1.4 \pm 0.8 \mu\text{m}/\text{min}$  and grow or shrink at the same rate, which is close to the shortening rate of puncta-stained contacts of  $1.6 \pm 0.6 \mu\text{m}/\text{min}$ . Importantly, occasional contacts where only diffuse Pk1 is present (Fig. 8 F) shorten significantly faster, at  $3.9 \pm 0.3 \mu\text{m}/\text{min}$  (Fig. 8 J).

An effect of punctate Pk1 on tail retraction is also indicated by the geometry of the two separating cell surfaces. Puncta-bearing tails are more pointed than the front ends of the cells they detach from, and the tail surface forms a smaller angle with the contact (Fig. 8 G). When Pk1 patches are absent, the surfaces of both cells tend to be pointed, and the respective contact-surface angles are similar to those of punctate tails (Fig. 8 H). Moreover, the angle between separating cells is larger (Fig. 8 I). The overall deformation of front and back cells is increased in puncta-less contacts, as is the rate of separation (Fig. 8 J). Apparently, diffuse Pk1 is sufficient for tail retraction, but puncta do affect the geometry and kinetics of cell separation.

Punctate Pk1 also affects the F-actin cortex, but in an unexpected way. Pk1 plaques and dense F-actin both accumulate at the trailing edge, but they are not colocalized: plaques alternate with F-actin (Fig. 9, A and A'). Consistent with a reduced cortex thickness at puncta, the whole Pk1-filled ER-free zone is narrower at puncta compared with regions of diffuse Pk1 (Fig. S3), suggesting that F-actin cortex is locally replaced in part by dense Pk1 condensate. An alternating arrangement of Pk1 plaques and F-actin is also seen in PCM explants treated with the Arp2/3 inhibitor CK666 (Fig. 9 B). Cells showed arrays of actin bundles that surround F-actin-depleted regions. Enormous Pk1 plaques are observed in these regions, as if plaques and F-actin were mutually exclusive.

### Pk1 puncta can be induced by cell deformation and osmotic stress

If cell deformation and associated mechanical stresses triggered Pk1 puncta formation, no direct and specific cell-to-cell signaling, as when Fz-Dvl interacted with Vangl-Pk, would be required. Consistent with this possibility, puncta and large plaques can occur on free cell surfaces. Viewed in the plane of the membrane, they appear as variably sized, irregular Pk1

aggregations that can change positions and occasionally fuse (Fig. 10 A). Moreover, cell spreading on a noncellular substrate prompts puncta formation. In dissociated cells placed on fibronectin (FN), small Pk1 puncta were induced within minutes (Fig. 10 B), although in small numbers (Fig. 10 C). Nonspecific adhesion to tissue plastic surface induced high numbers of medium-sized puncta that changed dynamically with time (Fig. 10, B and C). Apparently, formation of Pk1 puncta is triggered by cell deformation rather than molecular interactions at contacts via, e.g., interacting transmembrane PCP components.

To test the possibility that in the absence of large-scale cell deformation, mechanical stress is sufficient to induce puncta, osmotic pressure was exerted on single PCM cells (Fig. 10, D-G). Hypotonic buffer is frequently used to artificially increase cortical tension by osmotic swelling. This approach showed for example that Par-3 puncta in the cortex of *Caenorhabditis elegans* zygotes can be induced by mechanical force (Wang et al., 2017). However, when PCM cells were transferred from normal to quarter-strength buffer, no puncta formed (Fig. 10, D and E). Instead, puncta were induced within minutes in double-concentrated buffer, at the surface of most cells but also in the cytoplasm (Fig. 10 D). Their numbers and sizes (Fig. 10, E-G) were comparable to those in small PCM tissue fragments. Increasing osmotic pressure by incubating cells in sorbitol induced puncta of similar abundance and size in an even higher proportion of cases (Fig. 10, D-G). That puncta are induced in hyperosmotic conditions suggests that Pk1 condensation would require cell surface compression, not stretching like Par-3 puncta formation.

## Discussion

In *Xenopus* gastrula PCM cells, the diffuse cytoplasmic form of Pk1, together with Dvl2 and CKII, regulates the F-actin content of the cortex and hence cortical tension. CKII physically interacts with Pk1 (Daulat et al., 2012) and coprecipitates with Dvl (Willert et al., 1997) and could thus bind directly to Pk1 and Dvl2 to translate their relative activities into a quantitative modulation of overall cortex strength. In blebbing cells, Pk1-Dvl2-CKII-sensitive assembly of cortical F-actin occurs at the cell membrane. Regulation of membrane-localized phosphatase and tensin homolog (PTEN) by CKII and Arp2/3-based actin polymerization downstream of PTEN (Patsoukis et al., 2013; Tsujita and Itoh, 2015) would be a mechanism that restricts the potentially ubiquitous Pk1-Dvl2 activity to the membrane. That inhibition of Arp2/3 but not formin strongly disrupts the cortex in PCM cells would be consistent with Pk1-Dvl2-CKII acting upstream of Arp2/3. However, potential crosstalk between Arp2/3 and formins via competition for actin monomers or via small GTPase signaling (Chesarone and Goode, 2009;

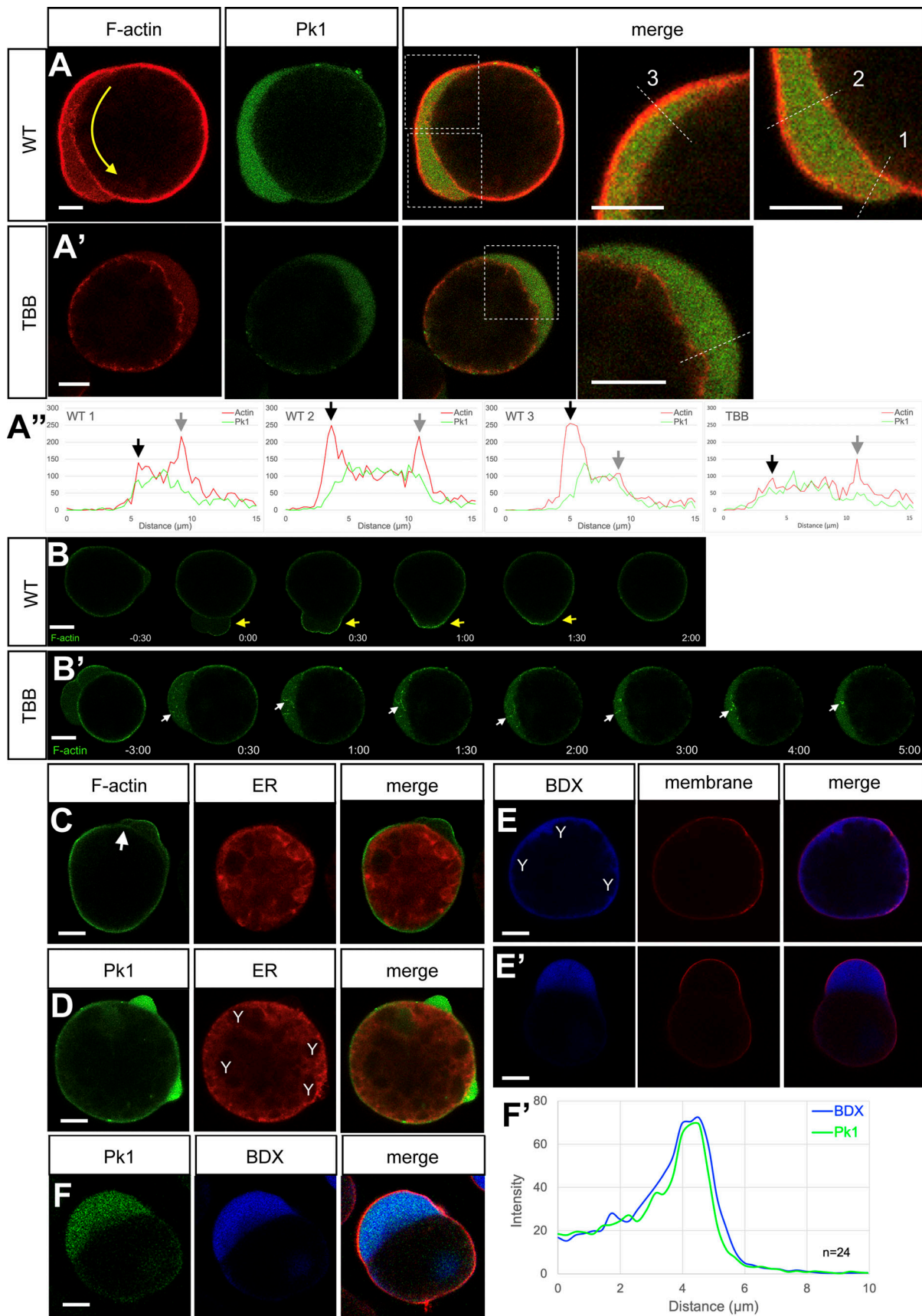


Figure 5. **PK1-Dvl2-CKII regulates F-actin dynamics at the cell membrane.** (A and A') PCM cells labeled with LifeAct-Ruby and Pk1-venus showing membrane blebs. In WT (A), a bleb forms near the bottom and retracts near the top, creating a circular movement (arrow). In the TBB-treated cell (A'), the bleb

forms a wide crescent. Right, enlargements of boxed areas. Scale bars, 10  $\mu\text{m}$ . **(A'')** Intensity plots of F-actin and Pk1 at dotted lines in A and A'. Black arrows, positions of membrane-attached cortex; gray arrows, cell body surface. **(B and B')** Time-series of LifeAct-GFP-labeled WT (B; Video 3) and TBB-treated (B'; Video 4) cells. Time in minutes. TBB was added at time 0:00. Yellow arrows, F-actin assembly at detached membrane; white arrows, newly assembled actin filaments in bleb. Scale bars, 10  $\mu\text{m}$ . **(C)** Live PCM cells labeled with LifeAct-GFP and ER-Tracker Red. Inner cortex layer at bleb (arrow) conforms to the ER domain. Scale bar, 10  $\mu\text{m}$ . **(D)** Live PCM cells labeled with Pk1-venus and ER-Tracker Red. Diffuse Pk1 appears enriched at cortex and in blebs but also fills cytoplasm; Y, yolk platelets. Scale bar, 10  $\mu\text{m}$ . **(E and E')** Live PCM cells labeled with blue dextran (BDX) and mb-RFP; Y, yolk platelets. Scale bars, 10  $\mu\text{m}$ . **(F)** Live PCM cells labeled with Pk1-venus, BDX, and mb-RFP. Scale bar, 10  $\mu\text{m}$ . **(F')** Average intensity line plot of Pk1 and BDX across the cell periphery (cell interior to the left;  $n = 24$ ).  $n$ , number of cells.

Rotty and Bear, 2015) must be considered, as inhibition of neither factor alone reproduces the effects of Pk1-Dvl2-CKII inhibition.

The cortex is also linked to the ER domain surface, as seen when it is split into layers in blebs or upon formin inhibition. Firm attachment between a dense subcortical ER and the actin cortex has previously been observed in *Xenopus* eggs during “cortical rotation,” where the F-actin sheet is moved relative to the yolk-filled deep cytoplasm by the kinesin-dependent translocation of the associated peripheral ER (Houliston and Elinson, 1991). Another cortex-ER link underlies the F-actin-dependent parallel retrograde movement of cell surface-attached beads, microtubules, and ER in *Xenopus* A6 cells (Terasaki and Reese, 1994). In a regulatory role, subcortical ER recruited to the cortex of a cell’s trailing edge can generate  $\text{Ca}^{2+}$  gradients to activate actomyosin contraction (Witze et al., 2013). Thus, the ER domain surface should be considered a significant determinant of cell mechanics, and the molecular mechanism of cortex-ER interaction of respective interest.

At the ER domain surface, F-actin is not assembled, and any remnants of a cortex are rapidly dissolved in normal and TBB-inhibited blebs. A simple interpretation would be that the cortex is assembled at the membrane and gradually disassembled as it moves away from the membrane, implying an inward flow of F-actin from cell membrane to ER domain surface. A Pk1-Dvl2-CKII-independent form of cortical F-actin is seen only in Pk1-Dvl2-CKII-inhibited cells. In blebs, its assembly is membrane independent, and it is stable on the ER domain surface. Since no stable residue of the cortex occurs in untreated blebs, this structure is possibly an inhibition artifact.

The actomyosin cortex integrates diverse signals into a unified mechanical response—cortical tension, whose spatial and temporal modulation determines cell shapes, motility, and adhesion (Kashkooli et al., 2021). Some of the input signals could originate from PCP pathways. In *Xenopus*, cortical tension regulation is involved in ectoderm-mesoderm boundary formation (Canty et al., 2017), a process that requires Dvl2 and Pk1 downregulation at the boundary (Luu et al., 2015). Importantly, in many cells, adhesion strength corresponds to a difference between cortical tensions at free and contacting cell surfaces (Brodland and Chen, 2000; Foty and Steinberg, 2005; Manning et al., 2010; Winklbauer, 2015), and in *Xenopus* ectoderm, the adhesion molecule C-cadherin regulates this tension differential (David et al., 2014). Pk1 and Dvl2 knockdown likewise affect the respective tensions, and thus adhesion strength measured as tissue surface tension.

In Pk1 morphants, adhesion strength is reduced, which seems at odds with an attenuation of cell rearrangement: lower

adhesion is equivalent to less work being required for cell separation and should thus facilitate rearrangement that involves the orderly detachment of cells from each other. However, adhesion strength and resistance to cell rearrangement are in general not proportionally affected by modulations of cortical tension (David et al., 2014). Mesenchymal cell migration, as in the PCM, includes a pulling forward of the transiently stretched cell body behind the leading edge (Ridley et al., 2003; Cramer, 2013). If pulling and the retraction of the rear end were more severely affected by low cortical tension than adhesion, this may lead to excessive cell stretching instead of cell detachment and translocation, and forming retraction fibers may be viewed as an extreme form of cell elongation due to weak cortex contractility.

Diffuse Pk1 is not obviously graded, and inhibiting Pk1 leaves cells still largely oriented toward the ectoderm, arguing for a role of Pk1 in uniform cell contractility rather than polarity. This seems to be different in the chordamesoderm, where PCP signaling polarizes cells. There, mediolateral intercalation of bipolar cells drives convergent extension. Pk2 puncta and Dvl2 are asymmetrically localized, and inhibiting their function leads to a loss of cell polarity and directional intercalation (Wallingford, 2012; Panousopoulou et al., 2013; Shindo et al., 2019). In the PCM, on the other hand, unipolar cells intercalate radially by migrating in the same direction, oriented by ectodermal PDGF-A (Damm and Winklbauer, 2011). Thus, in the two mesoderm regions, cell intercalation differs, and different roles of PCP signaling would not be unexpected (Davey and Moens, 2017).

The enrichment of Pk1 puncta near the trailing edge of cells is best explained by their induction by mechanical stress, a phenomenon known from Par-3. This protein is diffusely distributed in the cytoplasm when in a closed conformation and localized in cortical puncta when in an open conformation (Liu et al., 2020). The transition is triggered by actomyosin contraction (Wang et al., 2017). The Pk1 protein with its flexible Prickle Espinas Testin domain (Sweede et al., 2008) and three self-interacting LIN-11 Isl1 MEC3 domains (Jenny et al., 2003; Ayukawa et al., 2014) could similarly switch between a closed conformation in the cytoplasm and an open form that condenses as puncta. The molecular mechanism that triggers a response to mechanical stress in the cortex remains to be elucidated. It should explain how Pk1 protein not bound initially to the F-actin cortex can nevertheless sense its stress status. Moreover, Pk1 puncta are deeply embedded in the cortex, requiring puncta and cortex turnover to be tightly linked. Turnover rates for cortex components are in the range of several seconds (Fritzsche et al., 2013). The appearance or disappearance of Pk1 puncta within 30 s is consistent with a rapid coordinated growth and dissolution of actin and Pk1 structures.

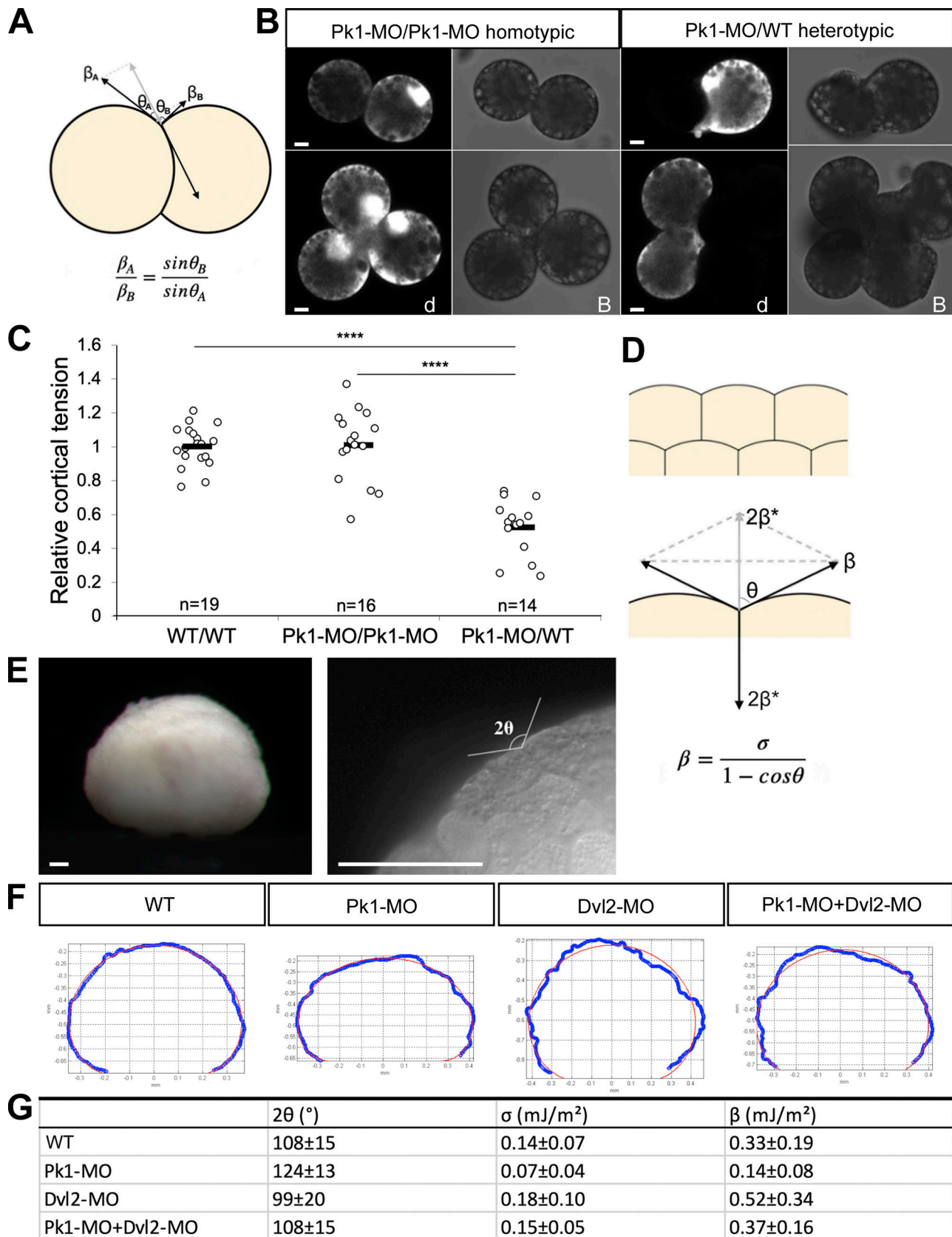


Figure 6. **Pk1-Dvl2-CKII regulates cell cortical tension.** (A) Schematic of cortical tensions  $\beta_A$  and  $\beta_B$  (arrows) and contributions  $\theta_A$  and  $\theta_B$  to contact angle of cell pair. (B) Homotypic Pk1-MO and heterotypic WT/Pk1-MO cell pairs showing straight and curved cell-cell boundaries, respectively. Pk1-MO cells labeled with blue dextran (d). B, bright field. Scale bars, 10  $\mu$ m. (C) Relative cortical tension  $\beta_A/\beta_B$  in WT homotypic ( $n = 19$ ), Pk1-MO homotypic ( $n = 16$ ), and

heterotypic ( $n = 14$ ) cell pairs and small clusters (2–15 cells).  $n$ , number of cell pairs or clusters. \*\*\*\*,  $P \leq 0.0001$  in a two-tailed Student's  $t$  test. Data distribution was assumed to be normal but was not formally tested. **(D)** Cell cortical tension  $\beta$ , tissue surface tension  $\sigma$ , and cell contact angle  $2\theta$  at the surface of a tissue. **(E)** An example of PCM aggregates, each from five to seven fused PCM explants, used to measure  $\sigma$  and  $2\theta$ . Scale bars, 100  $\mu\text{m}$ . **(F)** Aggregate outlines (blue) and best-fit curves (red) generated by the ADSA program. **(G)** Measured parameters  $2\theta$  and  $\sigma$  and calculated cortical tension  $\beta$ . WT,  $n = 21$ ; Pk1-MO,  $n = 8$ ; Dvl2-MO,  $n = 17$ ; Pk1-MO + Dvl2-MO,  $n = 6$ . Pk1-MO, 40 ng/bl; Dvl2-MO, 24 ng/bl. Means  $\pm$  SD are indicated.

Puncta formation is a possible mechanism to control Pk1 activity. Instead of further increasing F-actin in proportion to their increased Pk1 levels, Pk1 plaques are sites of localized depletion of cortical F-actin. Sequestering Pk1 protein into puncta or plaques could simply remove it from interaction with CKII, allowing the inhibitory Dvl2 to dominate. Dvl2 puncta could have the opposite effect, to locally remove diffuse Dvl2 protein

from the Pk1/Dvl2 equilibrium and shift the balance to Pk1 activity. This in turn would activate CKII and hence F-actin assembly.

The role of Pk1 puncta in cell separation needs to be further examined. Separation of *Xenopus* mesoderm cells involves the peeling of cells off each other, the shrinkage of contact areas, and cytoplasmic rupture (Wen and Winklbauer, 2017). A working

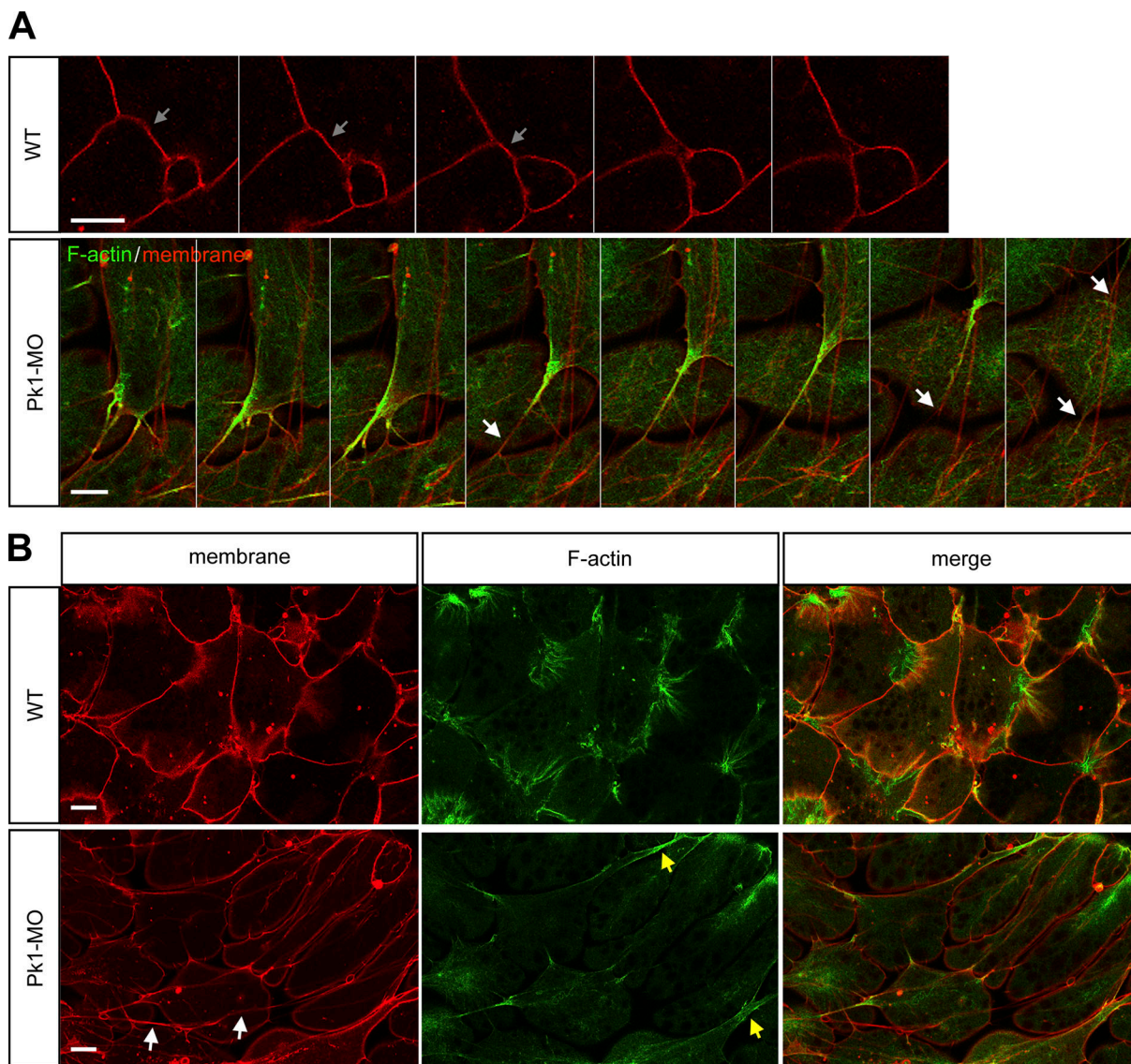


Figure 7. **Pk1 knockdown impairs rear-end retraction.** **(A)** From Video 6. Separating cells in WT (mb-RFP) and Pk1-MO (mb-RFP and LifeAct-GFP) PCM. BCR to the right. In WT, cell-cell contact shrinks (arrows). In Pk1 morphant, F-actin accumulates in retraction fiber and eventually recoils within membranes (arrows). Scale bars, 10  $\mu\text{m}$ . **(B)** WT and Pk1-MO PCM explants showing morphology and arrangement of mb-RFP- and LifeAct-GFP-labeled cells. BCR is to the right. In Pk1 morphant, F-actin free membrane tethers (white arrows) and F-actin filled retraction fibers (yellow arrows) connect former front-rear cell neighbors. Scale bars, 10  $\mu\text{m}$ .

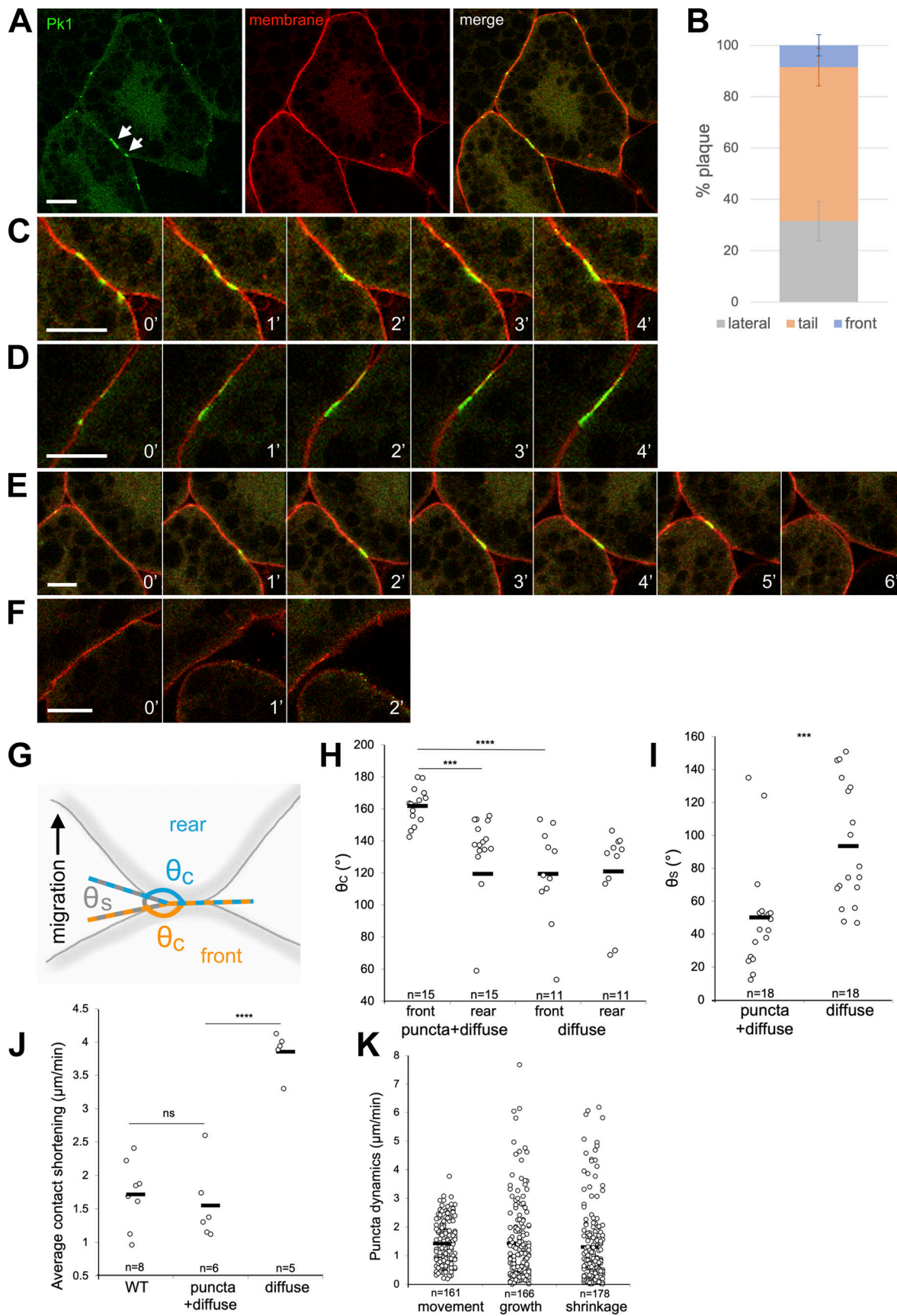


Figure 8. **Dynamic Pk1 puncta and plaques at separating cell-cell contacts.** (A) PCM expressing Pk1-venus and mb-RFP. Punctate Pk1 (arrows) at cell-cell contacts. BCR is to the top. Scale bar, 10  $\mu\text{m}$ . (B) Fractions of Pk1 plaques (>1  $\mu\text{m}$ ) at lateral cell contacts, cell tails, and front ends. Count of plaques was pooled

from multiple experiment replicates to calculate fractions. Error bars indicate SD.  $n = 225$ . **(C and D)** Dynamics of Pk1 puncta at cell contacts in PCM expressing Pk1-venus and mb-RFP. Time in minutes. Scale bars, 10  $\mu\text{m}$ . **(E and F)** Dynamics of separation at puncta-stained (E; Video 6) and puncta-less (F) cell contacts in PCM expressing Pk1-venus and mb-RFP. Time in minutes. Scale bars, 10  $\mu\text{m}$ . **(G)** Separation angle  $\theta_s$  and membrane curvature angle  $\theta_c$  at cell contact between front and rear ends of migrating PCM cells. **(H and I)** Membrane curvature angle  $\theta_c$  of each cell (puncta-stained contacts,  $n = 15$ ; puncta-less contacts,  $n = 11$ ) and contact angle  $\theta_s$  during tail retraction (puncta-stained contacts,  $n = 18$ ; puncta-less contacts,  $n = 18$ ). \*\*\*,  $P \leq 0.001$ ; \*\*\*\*,  $P \leq 0.0001$  in a two-tailed Student's  $t$  test. Data distribution was assumed to be normal but was not formally tested. **(J)** Rates of contact shortening during cell separation. Each data point represents the average changes of contact lengths from each contact over the period of separation (WT,  $n = 8$ ; puncta-stained,  $n = 6$ ; puncta-less,  $n = 5$ ). \*\*\*\*,  $P \leq 0.0001$  in a two-tailed Student's  $t$  test. Data distribution was assumed to be normal but was not formally tested. **(K)** Rates of puncta movement ( $n = 161$ ), growth ( $n = 166$ ), and shrinkage ( $n = 178$ ) at contacts, calculated by changes in puncta lengths.  $n$ , number of puncta.

hypothesis would assume that the relative prevalence of these mechanisms depends on the rate of cell separation. When contact shrinkage is too fast to be accommodated by normal actomyosin turnover, the cortex would be compressed. Under hyperosmotic conditions, a presumed cortex compression induces Pk1 puncta and plaques, which locally downregulate cortex strength. Such small-scale interruptions of the cortex at sites of cell deformation could moderate its pulling force and ensure tail retraction without formation of retraction fibers. The local downregulation of active RhoA by punctate Pk (Zhang et al., 2016) could also reduce pulling force in a parallel pathway via lowering myosin II activity.

## Materials and methods

### Embryos and microinjections

*X. laevis* embryos were fertilized in vitro in 1/10 $\times$  modified Barth's solution (MBS; 88 mM NaCl, 1 mM KCl, 2.4 mM NaHCO<sub>3</sub>, 0.82 mM MgSO<sub>4</sub>, 0.33 mM Ca[NO<sub>3</sub>]<sub>2</sub>, 0.41 mM CaCl<sub>2</sub>, 10 mM Hepes [+NaOH], 1% streptomycin, and 1% penicillin, pH 7.4). Fertilized embryos were dejellied with 2% cysteine in 1/10 $\times$  MBS with the pH adjusted to 8. Embryos were cultured in 1/10 $\times$  MBS in a 15°C incubator. Developing embryos were staged according to the Normal Table of *Xenopus* Development by Nieuwkoop and Faber (1967). Embryos were injected in 3% Ficoll in the equatorial region of dorsal blastomeres at 4-cell stage using pulled glass needles and a Nanoject II micro-injector (Drummond Scientific Company). Injected embryos were kept in 3% Ficoll for an hour to prevent cytoplasm loss and allow for healing. Embryos were then transferred to 1/10 $\times$  MBS and left to develop at 15°C until gastrula stages.

### Embryo bisections and lip explants

To check for effects on gastrulation, embryos at stage 10.5 were fixed with 4% formaldehyde for 2 h before midsagittal bisection along the dorsal-ventral axis using razor blades. Dorsal lip explants were excised from stage 10 embryos and kept in 1 $\times$  MBS to develop. Intact embryos from the same batch were used as a reference for staging. Explants at stage 10.5 were fixed with 4% formaldehyde for an hour before bisecting along the dorsal-ventral axis. Bisected embryos and explants were placed with the cut surface down in a dish and imaged using an inverted Zeiss Axiovert 200 M microscope.

### Preparation of substrata

Glass-bottom tissue culture dishes and glass coverslips were coated with 1 mg/ml BSA (1%) for 5 min to prevent attachment of

cells. For experiments on FN, dishes were coated with bovine plasma FN (Sigma-Aldrich) at 200 ng/ml for 30 min and saturated with 1% BSA in 1 $\times$  MBS for 5 min.

### Explants, tissue fragments, and dissociated cells

At gastrula stage 10.5, embryos were transferred to 1 $\times$  MBS, and the vitelline membrane was removed with forceps. PCM and BCR explants were excised from embryos at room temperature under a MZ16F Leica stereomicroscope. For examining whole PCM tissues, explants were plated on BSA-coated dishes and kept in 1 $\times$  MBS. Tissue fragments of different sizes were obtained by dissecting PCM explants into 1/4, 1/8, or 1/16. To dissociate cells, PCM explants were kept in calcium-free 1 $\times$  MBS (dissociation buffer; 88 mM NaCl, 1 mM KCl, 2.4 mM NaHCO<sub>3</sub>, 10 mM Hepes [+NaOH], 1% streptomycin, and 1% penicillin, pH 7.4) for 20 min. To observe single cells, cell pairs, and small aggregates of  $\leq 15$  cells, dissociated cells were transferred back to 1 $\times$  MBS in BSA-coated dishes for 20 min. To induce puncta, dissociated single cells were transferred to uncoated tissue culture plastic dishes or FN-coated dishes filled with 1 $\times$  MBS and left at room temperature for 20 min before imaging.

### PCM-BCR explant assays

A slice of PCM and attached endoderm and an explant of WT BCR were excised from stage 10.5 embryos and combined with the inner surface of the BCR facing the PCM. The explants were cultured in 1 $\times$  MBS on glass-bottom dishes and secured with a glass coverslip. They were filmed for 90 min at room temperature on a Zeiss Axiovert 200 M microscope with a 20 $\times$  air-immersion objective for tracking cell movements or on a Leica TCS SP8 laser scanning confocal microscope with a 40 $\times$  oil-immersion objective for visualizing fluorescence-labeled structures.

### Quantification of cell intercalation

The efficiency of PCM cell intercalation was quantified by counting the accumulated number of junction remodeling events over time. Each event is defined by the formation and expansion of a new anteroposterior cell-cell contact after complete mediolateral shrinking.

### Tracking and plotting cell movements

For analyzing cell migration and neighbor exchange, cell paths were tracked by following the center of cell body using the manual tracking plug-in on ImageJ. X and Y positions of each cell were recorded for plotting paths and for calculating translocation. Net translocation (NT) was calculated

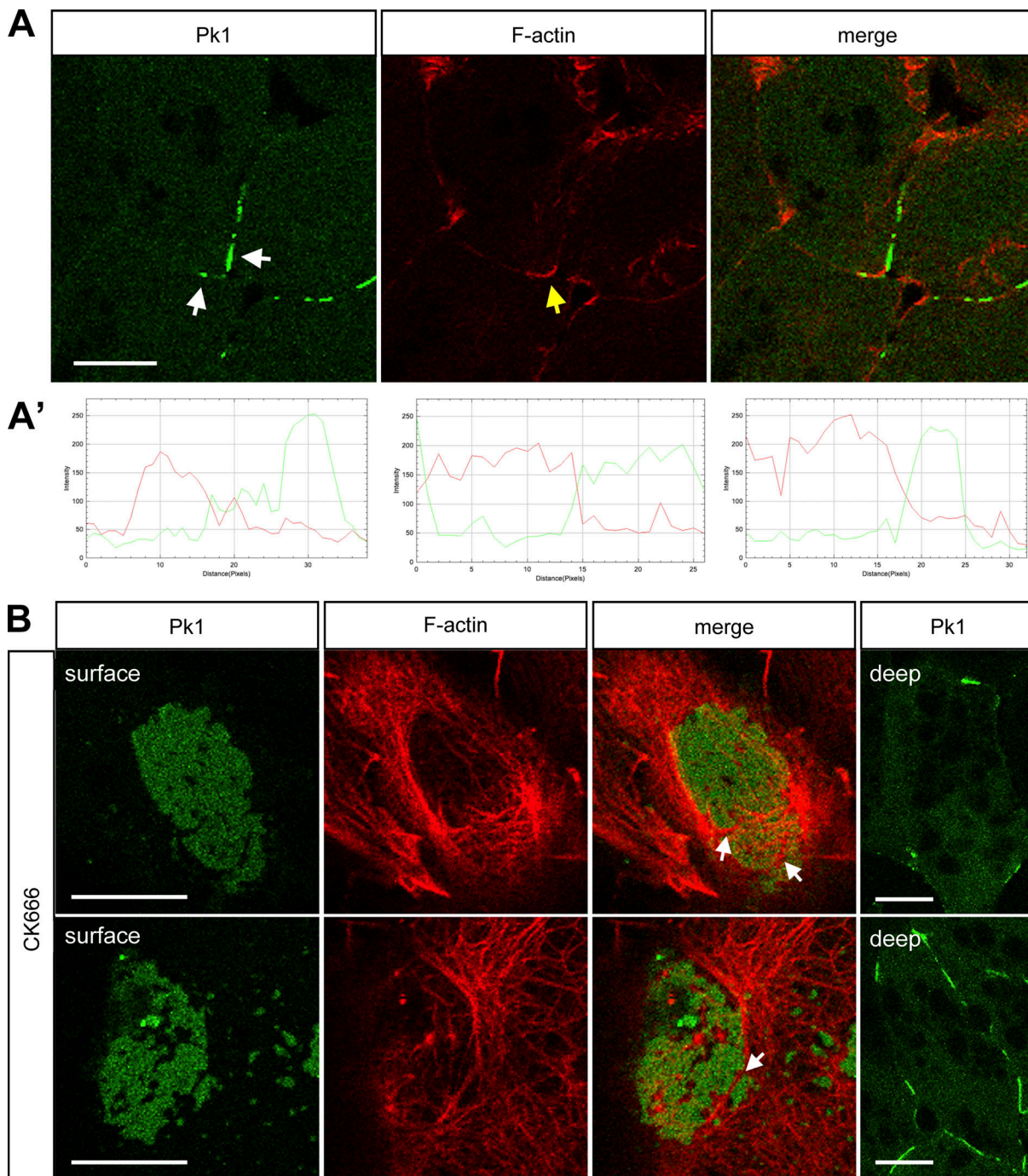


Figure 9. **Pk1 puncta alternate with F-actin densities.** **(A)** PCM expressing Pk1-venus and LifeAct-Ruby. Alternating localization of Pk1 plaques (white arrows) and F-actin dense regions (yellow arrows). Scale bar, 10  $\mu$ m. **(A')** Intensity plots of Pk1 (green) and F-actin (red) along cell membrane. **(B)** Cells in Pk1-venus and LifeAct-Ruby expressing PCM treated with Arp2/3 inhibitor CK666. Large Pk1 patches are surrounded by F-actin bundles (arrows). Below the surface, Pk1 plaques at cell-cell contacts; diffuse Pk1 distribution unchanged. Scale bars, 10  $\mu$ m.

by  $NT = \sqrt{(X_f - X_i)^2 + (Y_f - Y_i)^2}$ , where  $(X_i, Y_i)$  is the initial cell position and  $(X_f, Y_f)$  is the position of cell after rearrangement. Persistence was calculated by dividing NT by total distance travelled between consecutive frames over the duration of rearrangement. For showing cell velocity gradients, arrows with lengths proportional to velocity were drawn on the images of corresponding tissues at the onset of cell rearrangement using ImageJ.

#### Quantification of cell morphology and orientation

For quantifying cell stretching, the length and width of each cell were measured with the straight-line tool in ImageJ and used for calculating length/width ratios. Circularity of the cells was also measured using the freehand line tool on ImageJ. For quantifying cell orientation, the angle between cell leading edge and the BCR was measured and binned at 10° intervals. The percentage of angles in each bin was then calculated and plotted into a rose

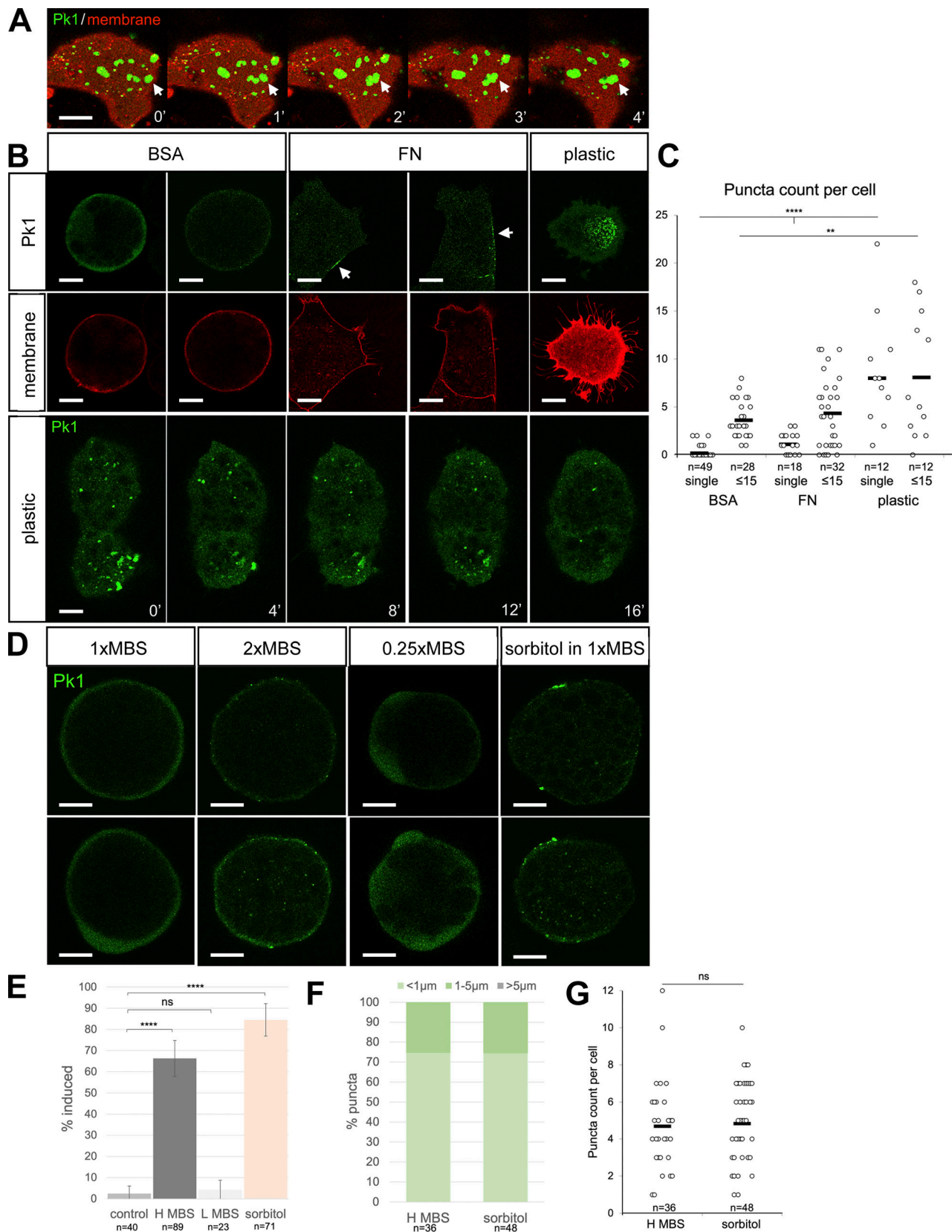


Figure 10. **Induction of Pk1 puncta.** (A) Pk1 puncta and plaque dynamics at surface of Pk1-venus- and mb-RFP-labeled PCM cells. Pk1 puncta/plaques can fuse (arrows). (B) Dissociated PCM cells labeled with Pk1-venus and mb-RFP on BSA, FN, and plastic. Arrows indicate Pk1 puncta outside the contact in cell pairs. Scale bars, 10  $\mu$ m. Time in minutes. Scale bars, 10  $\mu$ m. (C) Number of puncta per cell in single cells, pairs, and small clusters ( $\leq 15$  cells). On BSA: single cells,  $n = 49$ ; cell pairs and clusters,  $n = 28$ . On FN: single cells,  $n = 18$ ; cell pairs and clusters,  $n = 32$ . On plastic: single cells,  $n = 12$ ; cell pairs and clusters,  $n = 12$ .

*n*, number of cells. \*\*,  $P \leq 0.01$ ; \*\*\*\*,  $P \leq 0.0001$  in a two-tailed Student's *t* test. Data distribution was assumed to be normal but was not formally tested. **(D)** Single Pk1-venus-labeled PCM cells on BSA in 1× MBS, 2× MBS (H), 0.25× MBS (L), or 0.25 M sorbitol in 1× MBS. Scale bars, 10 μm. **(E)** Fraction of PCM cells showing Pk1 puncta formation. Count of puncta induced cells was pooled from multiple experiment replicates to calculate fractions. Control, *n* = 40; H MBS, *n* = 89; L MBS, *n* = 23; sorbitol, *n* = 71. *n*, number of cells. \*\*\*\*,  $P \leq 0.0001$  in a two-tailed Student's *t* test. Data distribution was assumed to be normal but was not formally tested. **(F)** Fractions of induced Pk1 puncta that are <1, 1–5, or >5 μm long in single PCM cells. Puncta count was pooled from multiple experiment replicates to calculate the fractions. H MBS, *n* = 36; sorbitol, *n* = 48. **(G)** Number of cell surface puncta per cell. H MBS, *n* = 36; sorbitol, *n* = 48. Two-tailed Student's *t* test. Data distribution was assumed to be normal but was not formally tested.

diagram using Rose Diagram Constructor, with 0 indicating the direction toward the BCR.

### Constructs, morpholinos, and inhibitors

Pk1-venus (a gift from S. Angers, University of Toronto, Canada; Daulat et al., 2012; cDNA for human Prickle1 was cloned into the pIRES-puro-VENUS pCS2+ vector) was injected at 200 pg per blastomere in both dorsal blastomeres for visualizing protein localization. Pk1-venus concentrations of 100, 200, 400, and 500 pg were injected to compare Pk1 localization. Concentrations <400 pg showed endogenous Pk1 distribution at different intensities, and those >400 pg showed additional puncta localization around the nucleus and have been used previously for functional overexpression studies (Daulat et al., 2012; Luu et al., 2015). For visualizing protein localization and rescuing/overexpression function, Pk1-venus was injected at 200 and 500 pg per blastomere, respectively. For mosaic Pk1 expression experiments, Pk1-venus was injected into only one of the dorsal blastomeres.

LifeAct-Ruby or LifeAct-GFP were gifts from M. Tada (University College London, UK) and C.-P. Heisenberg (Institute of Science and Technology Austria); pRuby-tagged or GFP-tagged LifeAct (Ibidi; Riedl et al., 2008) was cloned into the pCS2+ vector backbone. Injection was at 200 pg per blastomere to visualize F-actin. Membrane-bound RFP (a gift from N. Kinoshita, National Institute for Basic Biology, Okazaki, Japan; Iioka et al., 2004; a cDNA fragment of the COOH-terminal region of *Xenopus K-ras* was cloned by PCR and fused to RFP in pCS2+ vector) was injected at 200 pg per blastomere to visualize cell membranes. Pk1-MO (5'-TCACTTTGTCTCCGCCATTCTGCG-3'; Takeuchi et al., 2003; Daulat et al., 2012) and Dvl2-MO (5'-CTTCTGATCCATTTCCAAAGGCATG-3'; Sheldahl et al., 2003; Park et al., 2008) were obtained from Genetools. For single-cell phalloidin staining experiments, Pk1-MO was injected at 13, 27, and 40 ng per blastomere for low (L), medium (M), and high (H) concentrations, respectively, and Dvl2-MO was injected at 12, 24, and 36 ng per blastomere for low (L), medium (M), and high (H) concentrations, respectively. For all other experiments, Pk1-MO was injected at 40 ng and Dvl2-MO at 24 ng per blastomere. Blue dextran was injected at 34.5 ng per blastomere.

SMIFH2 (Rizvi et al., 2009; Isogai et al., 2015), CK666 (Hetrick et al., 2013), and TBB (Sarno et al., 2001; Pagano et al., 2008) were obtained from Sigma-Aldrich. SMIFH2 and CK666 were dissolved as 50 mM solution in DMSO and used at 2.5 μM for 20 min. TBB was dissolved as 100 μM solution in DMSO and used at 10 μM for 10 min. At this low concentration, off-target inhibition of myosin is minimal, at ~10% (Nishimura et al., 2021). ER-Tracker Red (catalog number E34250; Thermo

Fisher Scientific) was dissolved as 1 mM solution in DMSO and used at 1 μM.

### Phalloidin staining and cortex density measurements

Dissociated PCM cells were seeded on BSA-coated dishes and fixed with 4% formaldehyde. 5 min into the fixation, 10% Triton X-100 was added to 0.1% final concentration. Cells were fixed for an additional 15 min before washing with 1% BSA in 1× MBS (1% MBS/BSA). Fixed cells were stained with 5 μg/ml rhodamine-phalloidin (catalog number R415; Thermo Fisher Scientific) or Alexa Fluor 488-phalloidin (catalog number A12379; Thermo Fisher Scientific) for 20 min, washed in 1% MBS/BSA, and kept in 1× MBS. Dishes were divided into marked sections for cells with different treatments to ensure staining consistency. Uninjected cells were included in each dish for normalizing intensity measurements. Average intensity was calculated from pooled measurements of uninjected cells, and treated cells were all normalized to this average to calculate the percentage intensity. Cortex staining intensity was measured with the Axiovision outline tool. The plane of measurement at the cell's equator was determined by focusing through cells and selecting the plane where the cell diameter was maximal.

### Fluorescence microscopy

For visualizing Pk1, F-actin, cell membrane, or ER domain, glass coverslips were mounted over tissue explants or dissociated cells and secured with plasticine. Time-lapse recordings used for tracking cell migration and neighbor exchange were taken on a Carl Zeiss Axiovert 200M fluorescent microscope with a 20× air-immersion objective (NA = 0.55) using an AxioCam MDm camera and AxioVision 4.8 software. Images used for measuring actin intensity in single cells were taken on a Carl Zeiss Axiovert 200M fluorescent microscope with a 20× air immersion objective (NA = 0.55) using AxioCam MDm camera and AxioVision 4.8 software. Images used for measuring tissue surface tension were taken on a Carl Zeiss Stemi SV 11 with a 5× air-immersion objective using AxioCam MRc camera and AxioVision 4.8 software. Images used for measuring tissue surface contact angle were taken on a Carl Zeiss Axiovert 200M inverted microscope with a 20× air immersion objective (NA = 0.55) using AxioCam MDm camera and AxioVision 4.8 software. All other images and time-lapses were taken on a Leica TCS SP8 laser scanning confocal microscope with a 40× oil-immersion objective (NA = 1.3) using LasAF 3.2 software. All images and time-lapses were taken at room temperature.

### Quantification of Pk1, F-actin, and ER localization

Pk1-venus intensity was plotted at multiple locations along lines across the cell periphery for analyzing Pk1 localization in various

sized PCM aggregates. Punctate Pk1 was measured at puncta, and diffuse Pk1 was measured at regions free of puncta. Means of intensity were then calculated and plotted for each. Lengths of punctate Pk1 and cell perimeter were measured with ImageJ using the freehand line tool. Fraction of punctate was calculated by dividing the sum of puncta lengths in a cell by the cell perimeter. For comparing Pk1 and F-actin localizations in un-injected, SMIFH2-treated, and TBB-treated cells, intensities of Pk1-venus and LifeAct-Ruby were plotted along indicated lines in cells. The thickness of labeled diffuse Pk1 and F-actin zones and ER domain was measured with ImageJ using the straight-line tool.

### Quantification of relative and absolute cortical tensions

In homotypic and heterotypic cell pairs and clusters in MBS, contact angle components  $\theta_A$  and  $\theta_B$  were measured with the ImageJ angle tool and used for calculating relative cortical tensions. To calculate absolute cortical tensions, a group of five to seven PCM explants were fused into an aggregate and allow to round up for an hour in MBS and assume a drop shape on plasticine for a further 2 h. Aggregates were fixed with 4% formaldehyde before obtaining aggregate profiles by imaging aggregates from the side in a 45° mirror using a stereomicroscope and AxioCam MRC camera (Zeiss). Tissue surface tension was determined using ADSA (Río and Neumann, 1997; Luu et al., 2011, 2015) to fit the aggregate profiles thus obtained to theoretical drop-shape curves. The drop shape of a tissue aggregate represents an equilibrium state of balanced tissue surface tension  $\sigma$  and gravity, which rounds up and flattens the tissue, respectively. The ADSA program generates theoretical drop shapes of different surface tensions using the Laplace equation and finds the best fit to measured aggregate outlines. After ADSA measurements, aggregates were cut in half and laid flat in glass-bottom dishes for measuring tissue surface contact angles using the Axiovision angle tool.

### Quantification of cell separation

Cell contact angles  $\theta_c$  for cell front and rear ends were measured for fluorescence-labeled cell membranes using the angle tool in ImageJ. Cell separation angles  $\theta_s$  were measured between detaching membranes using the same tool. Contact shortening rates were quantified by measuring contact lengths in successive frames using the freehand tool in ImageJ and calculating the average of length changes between consecutive frames for each separating contact. Puncta movement, growth, and shrinkage rates were measured similarly for each punctum. Cell–cell contacts that were free of Pk1 puncta throughout contact shortening and detachment were used for measuring diffuse-only contacts, and all other contacts were categorized as punctate.

### Osmotic stress treatments

Dissociated PCM cells were transferred to 2× MBS (166 mM NaCl, 2 mM KCl, 4.6 mM NaHCO<sub>3</sub>, 1.64 mM MgSO<sub>4</sub>, 0.66 mM Ca [NO<sub>3</sub>]<sub>2</sub>, 0.82 mM CaCl<sub>2</sub>, 20 mM Hepes [+NaOH], 2% streptomycin, and 2% penicillin, pH 7.4) or 0.25 M sorbitol in 1× MBS to increase osmolarity, or to 0.25× MBS (22 mM NaCl, 0.25 mM KCl, 0.6 mM NaHCO<sub>3</sub>, 0.21 mM MgSO<sub>4</sub>, 0.08 mM Ca[NO<sub>3</sub>]<sub>2</sub>, 0.10 mM CaCl<sub>2</sub>, 2.5 mM Hepes [+NaOH], 0.25% streptomycin,

and 0.25% penicillin, pH 7.4) to reduce osmolarity. Cells were incubated for 20 min before imaging.

### Pk1 immunostaining

PCM tissues were dissected from stage 10.5 embryos, fixed with 4% paraformaldehyde, and incubated in 1% BSA in 1× PBS for an hour. Fixed tissues were incubated at 4°C overnight in rabbit polyclonal IgG anti-Prickle (1:50 dilution; ab15577; Abcam) primary antibody in 1% BSA in PBS, washed three times with 1% BSA in 1× PBS, and then incubated in a 1:200 dilution of FITC-goat anti-rabbit IgG secondary antibody (code number 111-095-144; Jackson ImmunoResearch Laboratories) for an hour at room temperature. Stained tissues were washed in 1% BSA in 1× MBS, placed on BSA-coated glass-bottom dishes, and secured with a coverslip for imaging.

### Statistical analysis

Statistical analyses were performed using two-tailed unpaired Student's *t* tests to compare different populations on GraphPad *t* test calculator. Statistical significance was indicated by \*,  $P \leq 0.05$ ; \*\*,  $P \leq 0.01$ ; \*\*\*,  $P \leq 0.001$ ; and \*\*\*\*,  $P \leq 0.0001$ . Data distribution was assumed to be normal but was not formally tested. Relative error of cortical tension  $\beta$  was calculated by propagation of uncertainty using the equation  $\Delta\beta = \sqrt{\frac{\sigma^2\Delta^2\theta\sin^2\theta + \Delta^2\sigma(\cos\theta - 1)^2}{(\cos\theta - 1)^4}}$ , where  $\Delta\sigma$  is SD of surface tension  $\sigma$  and  $\Delta\theta$  is SD of half of the contact angle  $2\theta$ .

### Online supplemental material

Fig. S1 shows gastrulation phenotypes in embryos and lip explants. Fig. S2 shows endogenous Pk expression in the PCM shown by Pk1 antibody staining. Fig. S3 shows that Pk1 is enriched at the ER-free cell periphery in PCM tissue mosaically labeled with Pk1-venus and ER-Tracker Red. Video 1 shows cell migration and radial intercalation in a WT PCM explant. Video 2 shows cell movements in a Pk1 morphant PCM explant. Video 3 shows bleb formation and retraction in a nonattached PCM cell. Video 4 shows bleb collapsed after TBB treatment in a PCM cell. Video 5 shows cell tail retraction in Pk1 morphant PCM tissue. Video 6 shows dynamics of Pk1 puncta at separating PCM cell contacts. All videos are shown at 25 frames per second.

### Acknowledgments

This work was supported by the Canadian Institutes of Health Research (PJT-15614).

The authors declare no competing financial interests.

Author contributions: Conceptualization: Y. Huang, R. Winklbauer; Formal analysis: Y. Huang; Funding acquisition: R. Winklbauer; Investigation: Y. Huang; Project administrations: R. Winklbauer; Resources: R. Winklbauer; Supervision: R. Winklbauer; Writing—original draft: Y. Huang, R. Winklbauer; Writing—review and editing: Y. Huang, R. Winklbauer.

Submitted: 21 August 2020

Revised: 18 January 2022

Accepted: 9 April 2022

## References

- Adler, P.N. 2002. Planar signaling and morphogenesis in *Drosophila*. *Dev. Cell.* 2:525–535. [https://doi.org/10.1016/s1534-5807\(02\)00176-4](https://doi.org/10.1016/s1534-5807(02)00176-4)
- Amack, J.D., and M.L. Manning. 2012. Knowing the boundaries: Extending the differential adhesion hypothesis in embryonic cell sorting. *Science.* 338:212–215. <https://doi.org/10.1126/science.1223953>
- Ayukawa, T., M. Akiyama, J.L. Mummery-Widmer, T. Stoeger, J. Sasaki, J.A. Knoblich, H. Senoo, T. Sasaki, and M. Yamazaki. 2014. Dachshous-dependent asymmetric localization of spiny-legs determines Planar Cell Polarity orientation in *Drosophila*. *Cell Rep.* 8:610–621. <https://doi.org/10.1016/j.celrep.2014.06.009>
- Biro, M., Y. Romeo, S. Kroschwald, M. Bovellan, A. Boden, J. Tcherkezian, P.P. Roux, G. Charras, and E.K. Paluch. 2013. Cell cortex composition and homeostasis resolved by integrating proteomics and quantitative imaging. *Cytoskeleton.* 70:741–754. <https://doi.org/10.1002/cm.21142>
- Brodland, G.W., and H.H. Chen. 2000. The mechanics of heterotypic cell aggregates: Insights from computer simulations. *J. Biomech. Eng.* 122:402–407. <https://doi.org/10.1115/1.1288205>
- Butler, M.T., and J.B. Wallingford. 2018. Spatial and Temporal analysis of PCP protein dynamics during neural TUBE closure. *Elife.* 7:e36456. <https://doi.org/10.7554/elife.36456>
- Canton, D.A., M.E.K. Olsten, K. Kim, A. Doherty-Kirby, G. Lajoie, J.A. Cooper, and D.W. Litchfield. 2005. The pleckstrin homology domain-containing protein CKIP-1 is involved in regulation of cell morphology and the actin cytoskeleton and interaction with actin capping protein. *Mol. Cell Biol.* 25:3519–3534. <https://doi.org/10.1128/mcb.25.9.3519-3534.2005>
- Canty, L., E. Zarour, L. Kashkooli, P. François, and F. Fagotto. 2017. Sorting at embryonic boundaries requires high heterotypic interfacial tension. *Nat. Commun.* 8:157. <https://doi.org/10.1038/s41467-017-00146-x>
- Carreira-Barbosa, F., M.L. Concha, M. Takeuchi, N. Ueno, S.W. Wilson, and M. Tada. 2003. Prickle 1 regulates cell movements during gastrulation and neuronal migration in zebrafish. *Development.* 130:4037–4046. <https://doi.org/10.1242/dev.00567>
- Chesarone, M.A., and B.L. Goode. 2009. Actin nucleation and elongation factors: Mechanisms and interplay. *Curr. Opin. Cell Biol.* 21:28–37. <https://doi.org/10.1016/j.cob.2008.12.001>
- Chugh, P., and E.K. Paluch. 2018. The actin cortex at a glance. *J. Cell Sci.* 131: jcs186254. <https://doi.org/10.1242/jcs.186254>
- Ciruna, B., A. Jenny, D. Lee, M. Mlodzik, and A.F. Schier. 2006. Planar cell polarity signalling couples cell division and morphogenesis during neurulation. *Nature.* 439:220–224. <https://doi.org/10.1038/nature04375>
- Clark, A.G., K. Dierkes, and E.K. Paluch. 2013. Monitoring actin cortex thickness in live cells. *Biophys. J.* 105:570–580. <https://doi.org/10.1016/j.bpj.2013.05.057>
- Cramer, L.P. 2013. Mechanism of cell rear retraction in migrating cells. *Curr. Opin. Cell Biol.* 25:591–599. <https://doi.org/10.1016/j.cob.2013.05.001>
- Damm, E.W., and R. Winklbauer. 2011. PDGF-A controls mesoderm cell orientation and radial intercalation during *Xenopus* gastrulation. *Development.* 138:565–575. <https://doi.org/10.1242/dev.056903>
- Darken, R.S., A.M. Scola, A.S. Rakeeman, G. Das, M. Mlodzik, and P.A. Wilson. 2002. The planar polarity gene strabismus regulates convergent extension movements in *Xenopus*. *EMBO J.* 21:976–985. <https://doi.org/10.1093/emboj/21.5.976>
- Daulat, A.M., O. Luu, A. Sing, L. Zhang, J.L. Wrana, H. McNeill, R. Winklbauer, and S. Angers. 2012. Mink1 regulates  $\beta$ -catenin-independent Wnt signaling via Prickle phosphorylation. *Mol. Cell Biol.* 32:173–185. <https://doi.org/10.1128/mcb.06320-11>
- Davey, C.F., and C.B. Moens. 2017. Planar cell polarity in moving cells: Think globally, act locally. *Development.* 144:187–200. <https://doi.org/10.1242/dev.122804>
- David, R., O. Luu, E.W. Damm, J.W.H. Wen, M. Nagel, and R. Winklbauer. 2014. Tissue cohesion and the mechanics of cell rearrangement. *Development.* 141:3672–3682. <https://doi.org/10.1242/dev.104315>
- Evans, E., and A. Yeung. 1989. Apparent viscosity and cortical tension of blood granulocytes determined by micropipet aspiration. *Biophys. J.* 56:151–160. [https://doi.org/10.1016/S0006-3495\(89\)82660-8](https://doi.org/10.1016/S0006-3495(89)82660-8)
- Evren, S., J.W.H. Wen, O. Luu, E.W. Damm, M. Nagel, and R. Winklbauer. 2014. EphA4-dependent Brachyury expression is required for dorsal mesoderm involution in the *Xenopus* gastrula. *Development.* 141:3649–3661. <https://doi.org/10.1242/dev.111880>
- Fackler, O.T., and R. Grosse. 2008. Cell motility through plasma membrane blebbing. *J. Cell Biol.* 181:879–884. <https://doi.org/10.1083/jcb.200802081>
- Foty, R.A., and M.S. Steinberg. 2005. The differential adhesion hypothesis: A direct evaluation. *Dev. Biol.* 278:255–263. <https://doi.org/10.1016/j.ydbio.2004.11.012>
- Fritzsche, M., A. Lewalle, T. Duke, K. Kruse, and G. Charras. 2013. Analysis of turnover dynamics of the submembranous actin cortex. *Mol. Biol. Cell.* 24:757–767. <https://doi.org/10.1091/mbc.e12-06-0485>
- Gao, C., and Y.G. Chen. 2010. Dishevelled: The hub of Wnt signaling. *Cell Signal.* 22:717–727. <https://doi.org/10.1016/j.cellsig.2009.11.021>
- Gao, Y., and H.-y. Wang. 2006. Casein kinase 2 is activated and essential for Wnt/ $\beta$ -catenin signaling. *J. Biol. Chem.* 281:18394–18400. <https://doi.org/10.1074/jbc.m60112200>
- Gray, R.S., I. Roszko, and L. Solnica-Krezel. 2011. Planar cell polarity: Coordinating morphogenetic cell behaviors with embryonic polarity. *Dev. Cell.* 21:120–133. <https://doi.org/10.1016/j.devcel.2011.06.011>
- Heisenberg, C.-P., M. Tada, G.J. Rauch, L. Saúde, M.L. Concha, R. Geisler, D.L. Stemple, J.C. Smith, and S.W. Wilson. 2000. Silberblick/Wnt11 mediates convergent extension movements during zebrafish gastrulation. *Nature.* 405:76–81. <https://doi.org/10.1038/35011068>
- Hetrick, B., M.S. Han, L.A. Helgeson, and B.J. Nolen. 2013. Small molecules ck-666 and ck-869 inhibit actin-related protein 2/3 complex by blocking an activating conformational change. *Chem. Biol.* 20:701–712. <https://doi.org/10.1016/j.chembiol.2013.03.019>
- Houliston, E., and R.P. Elinson. 1991. Evidence for the involvement of microtubules, ER, and kinesin in the cortical rotation of fertilized frog eggs. *J. Cell Biol.* 114:1017–1028. <https://doi.org/10.1083/jcb.114.5.1017>
- Huang, Y., and R. Winklbauer. 2018. Cell migration in the *Xenopus* gastrula. *Wiley Interdiscip. Rev. Dev. Biol.* 7:1–21:E325. <https://doi.org/10.1002/wdev.325>
- Iioka, H., N. Ueno, and N. Kinoshita. 2004. Essential role of MARCKS in cortical actin dynamics during gastrulation movements. *J. Cell Biol.* 164:169–174. <https://doi.org/10.1083/jcb.200310027>
- Isogai, T., R.V. Kammen, and M. Innocenti. 2015. SMIFH2 has effects on Formins and p53 that perturb the cell cytoskeleton. *Sci. Rep.* 5:9802. <https://doi.org/10.1038/srep09802>
- Jenny, A., R.S. Darken, P.A. Wilson, and M. Mlodzik. 2003. Prickle and Strabismus form a functional complex to generate a correct axis during planar cell polarity signaling. *EMBO J.* 22:4409–4420. <https://doi.org/10.1093/emboj/cdg424>
- Jessen, J.R., J. Topczewski, S. Bingham, D.S. Sepich, F. Marlow, A. Chandrasekhar, and L. Solnica-Krezel. 2002. Zebrafish trilobite identifies new roles for Strabismus in gastrulation and neuronal movements. *Nat. Cell Biol.* 4:610–615. <https://doi.org/10.1038/ncb828>
- Kashkooli, L., D. Rozema, L. Espejo-Ramirez, P. Lasko, and F. Fagotto. 2021. Ectoderm to mesoderm transition by downregulation of actomyosin contractility. *PLoS Biol.* 19:e3001060. <https://doi.org/10.1371/journal.pbio.3001060>
- Kestler, H.A., and M. Kühl. 2008. From individual Wnt pathways toward a Wnt signalling network. *Philos. Trans. R. Soc. Lond. B Biol. Sci.* 363:1333–1347. <https://doi.org/10.1098/rstb.2007.2251>
- Kinoshita, N., H. Iioka, A. Miyakoshi, and N. Ueno. 2003. PKC delta is essential for Dishevelled function in a noncanonical Wnt pathway that regulates *Xenopus* convergent extension movements. *Genes Dev.* 17:1663–1676. <https://doi.org/10.1101/gad.1101303>
- Kramerov, A.A., K. Ahmed, and A.V. Ljubimov. 2012. Cell rounding in cultured human astrocytes and vascular endothelial cells upon inhibition of CK2 is mediated by actomyosin cytoskeleton alterations. *J. Cell Biochem.* 113:2948–2956. <https://doi.org/10.1002/jcb.24171>
- Lapébie, P., C. Borchiellini, and E. Houliston. 2011. Dissecting the PCP pathway: One or more pathways? Does a separate Wnt-Fz-Rho pathway drive morphogenesis? *Bioessays.* 33:759–768. <https://doi.org/10.1002/bies.201100023>
- Liu, Z., Y. Yang, A. Gu, J. Xu, Y. Mao, H. Lu, W. Hu, Q.-Y. Lei, Z. Li, M. Zhang, et al. 2020. PAR complex cluster formation mediated by phase separation. *Nat. Commun.* 11:2266. <https://doi.org/10.1038/s41467-020-16135-6>
- Luu, O., R. David, H. Ninomiya, and R. Winklbauer. 2011. Large-scale mechanical properties of *Xenopus* embryonic epithelium. *Proc. Natl. Acad. Sci. USA.* 108:4000–4005. <https://doi.org/10.1073/pnas.1010331108>
- Luu, O., E.W. Damm, S.E. Parent, D. Barua, T.H.L. Smith, J.W.H. Wen, S.E. Lepage, M. Nagel, H. Ibrahim-Gawel, Y. Huang, et al. 2015. PAPC mediates self/non-self-distinction during snail1-dependent tissue separation. *J. Cell Biol.* 208:839–856. <https://doi.org/10.1083/jcb.201409026>
- Manning, M.L., R.A. Foty, M.S. Steinberg, and E.-M. Schoetz. 2010. Coaction of intercellular adhesion and cortical tension specifies tissue surface tension. *Proc. Natl. Acad. Sci. USA.* 107:12517–12522. <https://doi.org/10.1073/pnas.1003743107>
- Nieuwkoop, P.D., and J. Faber. 1967. Normal Table of *Xenopus Laevis* (Daudin): A Systematical and Chronological Survey of the Development from

- the Fertilized Egg till the end of Metamorphosis. North-Holland Publishing Company, Amsterdam
- Nishimura, Y., S. Shi, F. Zhang, R. Liu, Y. Takagi, A.D. Bershadsky, V. Viasnoff, and J.R. Sellers. 2021. The formin inhibitor SMIFH2 inhibits members of the myosin superfamily. *J. Cell Sci.* 134:jcs253708. <https://doi.org/10.1242/jcs.253708>
- Pagano, M. A., J. Bain, Z. Kazimierczuk, S. Sarno, M. Ruzzene, G. Di Maira, M. Elliott, A. Orzeszko, G. Cozza, F. Meggio, and L. A. Pinna. 2008. The selectivity of inhibitors of protein kinase CK2: An update. *Biochem. J.* 415:353–365. <https://doi.org/10.1042/bj20080309>
- Panousopoulou, E., R.A. Tyson, T. Bretschneider, and J.B.A. Green. 2013. The distribution of Dishevelled in convergently extending mesoderm. *Dev. Biol.* 382:496–503. <https://doi.org/10.1016/j.ydbio.2013.07.012>
- Park, T.J., B.J. Mitchell, P.B. Abitua, C. Kintner, and J.B. Wallingford. 2008. Dishevelled controls apical docking and planar polarization of basal bodies in ciliated epithelial cells. *Nat. Genet.* 40:871–879. <https://doi.org/10.1038/ng.104>
- Pasternak, C., J.A. Spudich, and E.L. Elson. 1989. Capping of surface receptors and concomitant cortical tension are generated by conventional myosin. *Nature.* 341:549–551. <https://doi.org/10.1038/341549a0>
- Patsoukis, N., L. Li, D. Sari, V. Petkova, and V.A. Boussiotis. 2013. PD-1 increases PTEN phosphatase activity while decreasing PTEN protein stability by inhibiting casein kinase 2. *Mol. Cell Biol.* 33:3091–3098. <https://doi.org/10.1128/MCB.00319-13>
- Ridley, A.J., M.A. Schwartz, K. Burridge, R.A. Firtel, M.H. Ginsberg, G. Borisy, J.T. Parsons, and A.R. Horwitz. 2003. Cell migration: Integrating signals from front to back. *Science.* 302:1704–1709. <https://doi.org/10.1126/science.1092053>
- Riedl, J., A.H. Crevenna, K. Kessenbrock, J.H. Yu, D. Neukirchen, M. Bista, F. Bradke, D. Jenne, T.A. Holak, Z. Werb, et al. 2008. Lifeact: A versatile marker to visualize F-actin. *Nat. Methods.* 5:605–607. <https://doi.org/10.1038/nmeth.1220>
- Rizvi, S.A., E.M. Neidt, J. Cui, Z. Feiger, C.T. Skau, M.L. Gardel, S.A. Kozmin, and D.R. Kovar. 2009. Identification and characterization of a small molecule inhibitor of Formin-mediated actin assembly. *Chem. Biol.* 16:1158–1168. <https://doi.org/10.1016/j.chembiol.2009.10.006>
- Río, O., and A. Neumann. 1997. Axisymmetric drop shape analysis: Computational methods for the measurement of interfacial properties from the shape and dimensions of pendant and sessile drops. *J. Colloid Interface Sci.* 196:136–147. <https://doi.org/10.1006/jcis.1997.5214>
- Rotty, J.D., and J.E. Bear. 2015. Competition and collaboration between different actin assembly pathways allows for homeostatic control of the actin cytoskeleton. *Bioarchitecture.* 5:27–34. <https://doi.org/10.1080/19490992.2015.1090670>
- Salbreux, G., G. Charras, and E. Paluch. 2012. Actin cortex mechanics and cellular morphogenesis. *Trends Cell Biol.* 22:536–545. <https://doi.org/10.1016/j.tcb.2012.07.001>
- Sarno, S., H. Reddy, F. Meggio, M. Ruzzene, S.P. Davies, A. Donella-Deana, D. Shugar, and L.A. Pinna. 2001. Selectivity of 4,5,6,7-tetrabromobenzotriazole, an ATP site-directed inhibitor of protein kinase CK2 ('casein kinase-2'). *FEBS Letters.* 496:44–48. [https://doi.org/10.1016/s0014-5793\(01\)02404-8](https://doi.org/10.1016/s0014-5793(01)02404-8)
- Sheldahl, L.C., D.C. Slusarski, P. Pandur, J.R. Miller, M. Kühl, and R.T. Moon. 2003. Dishevelled activates Ca<sup>2+</sup> flux, PKC, and CamKII in vertebrate embryos. *J. Cell Biol.* 161:769–777. <https://doi.org/10.1083/jcb.200211094>
- Shindo, A., Y. Inoue, M. Kinoshita, and J.B. Wallingford. 2019. PCP-dependent transcellular regulation of actomyosin oscillation facilitates convergent extension of vertebrate tissue. *Dev. Biol.* 446:159–167. <https://doi.org/10.1016/j.ydbio.2018.12.017>
- Strutt, D. 2003. Frizzled signalling and cell polarisation in Drosophila and vertebrates. *Development.* 130:4501–4513. <https://doi.org/10.1242/dev.00695>
- Strutt, H., S.J. Warrington, and D. Strutt. 2011. Dynamics of core planar polarity protein turnover and stable assembly into discrete membrane subdomains. *Dev. Cell.* 20:511–525. <https://doi.org/10.1016/j.devcel.2011.03.018>
- Strutt, H., J. Gamage, and D. Strutt. 2016. Robust asymmetric localization of planar polarity proteins is associated with organization into signalosome-like domains of variable stoichiometry. *Cell Rep.* 17:2660–2671. <https://doi.org/10.1016/j.celrep.2016.11.021>
- Sweede, M., G. Ankem, B. Chutvirasakul, H.F. Azurmendi, S. Chbeir, J. Watkins, R.F. Helm, C.V. Finkielstein, and D.G.S. Capelluto. 2008. Structural and membrane binding properties of the Prickle pet domain. *Biochemistry.* 47:13524–13536. <https://doi.org/10.1021/bi801037h>
- Tada, M., and M. Kai. 2009. Noncanonical Wnt/PCP signaling during vertebrate gastrulation. *Zebrafish.* 6:29–40. <https://doi.org/10.1089/zeb.2008.0566>
- Tada, M., and J.C. Smith. 2000. Xwnt11 is a target of Xenopus Brachyury: Regulation of gastrulation movements via Dishevelled, but not through the canonical Wnt pathway. *Development.* 127:2227–2238. <https://doi.org/10.1242/dev.127.10.2227>
- Takeuchi, M., J. Nakabayashi, T. Sakaguchi, T.S. Yamamoto, H. Takahashi, H. Takeda, and N. Ueno. 2003. The Prickle-related gene in vertebrates is essential for gastrulation cell movements. *Curr. Biol.* 13:674–679. [https://doi.org/10.1016/s0960-9822\(03\)00245-8](https://doi.org/10.1016/s0960-9822(03)00245-8)
- Terasaki, M., and T.S. Reese. 1994. Interactions among endoplasmic reticulum, microtubules, and retrograde movements of the cell surface. *Cell Motil. Cytoskeleton.* 29:291–300. <https://doi.org/10.1002/cm.970290402>
- Tsujita, K., and T. Itoh. 2015. Phosphoinositides in the regulation of actin cortex and cell migration. *Biochim. Biophys. Acta.* 1851:824–831. <https://doi.org/10.1016/j.bbali.2014.10.011>
- van Amerongen, R., and R. Nusse. 2009. Towards an integrated view of Wnt signaling in development. *Development.* 136:3205–3214. <https://doi.org/10.1242/dev.033910>
- Veeman, M.T., J.D. Axelrod, and R.T. Moon. 2003. A second canon: Functions and mechanisms of  $\beta$ -catenin-independent Wnt signaling. *Dev. Cell.* 5:367–377. [https://doi.org/10.1016/s1534-5807\(03\)00266-1](https://doi.org/10.1016/s1534-5807(03)00266-1)
- Wallingford, J.B. 2012. Planar cell polarity and the developmental control of cell behavior in vertebrate embryos. *Annu. Rev. Cell Dev. Biol.* 28:627–653. <https://doi.org/10.1146/annurev-cellbio-092910-154208>
- Wallingford, J. B., and R. Habas. 2005. The developmental biology of Dishevelled: An enigmatic protein governing cell fate and cell polarity. *Development.* 132:4421–4436. <https://doi.org/10.1242/dev.02068>
- Wallingford, J.B., B.A. Rowning, K.M. Vogeli, U. Rothbacher, S.E. Fraser, and R.M. Harland. 2000. Dishevelled controls cell polarity during Xenopus gastrulation. *Nature.* 405:81–85. <https://doi.org/10.1038/35011077>
- Wang, S.-C.S., T.Y.F. Low, T.Y., L. Low, Y. Gole, W. Nishimura, and F. Yu-Motegi. 2017. Cortical forces and CDC-42 control clustering of Par proteins for *C. elegans* embryonic polarization. *Mech. Dev.* 145:988–995. <https://doi.org/10.1016/j.mod.2017.04.243>
- Wen, J.W., and R. Winklbauer. 2017. Ingression-type cell migration drives vegetal endoderm internalisation in the *Xenopus* gastrula. *Elife.* 6:e27190. <https://doi.org/10.7554/eLife.27190>
- Willert, K., M. Brink, A. Wodarz, H. Varmus, and R. Nusse. 1997. Casein kinase 2 associates with and phosphorylates Dishevelled. *EMBO J.* 16:3089–3096. <https://doi.org/10.1093/emboj/16.11.3089>
- Winklbauer, R. 2015. Cell adhesion strength from cortical tension: An integration of concepts. *J. Cell Sci.* 128:3687–3693. <https://doi.org/10.1242/jcs.174623>
- Witze, E.S., M.K. Connacher, S. Houel, M.P. Schwartz, M.K. Morphew, L. Reid, D.B. Sacks, K.S. Anseth, and N.G. Ahn. 2013. Wnt5a directs polarized calcium gradients by recruiting cortical endoplasmic reticulum to the cell trailing edge. *Dev. Cell.* 26:645–657. <https://doi.org/10.1016/j.devcel.2013.08.019>
- Xavier, C.P., R.H. Rastetter, M. Blömacher, M. Stumpf, M.M. Himmel, R.O. Morgan, M.-P. Fernandez, C. Wang, A. Osman, Y. Miyata, et al. 2012. Phosphorylation of CRN2 by CK2 regulates F-actin and Arp2/3 interaction and inhibits cell migration. *Sci. Rep.* 2:241. <https://doi.org/10.1038/srep00241>
- Yin, C., M. Kiskowski, P.A. Pouille, E. Farge, and L. Solnica-Krezel. 2008. Cooperation of polarized cell intercalations drives convergence and extension of presomitic mesoderm during zebrafish gastrulation. *J. Cell Biol.* 180:221–232. <https://doi.org/10.1083/jcb.200704150>
- Zaidel-Bar, R., G. Zhenhuan, and C. Luxenburg. 2015. The contractome: A systems view of actomyosin contractility in non-muscle cells. *J. Cell Sci.* 128:2209–2217. <https://doi.org/10.1242/jcs.170068>
- Zhang, L., V. Luga, S.K. Armitage, M. Musiol, A. Won, C.M. Yip, S.V. Plotnikov, and J.L. Wrana. 2016. A lateral signalling pathway coordinates shape volatility during cell migration. *Nat. Commun.* 7:11714. <https://doi.org/10.1038/ncomms11714>

## Supplemental material

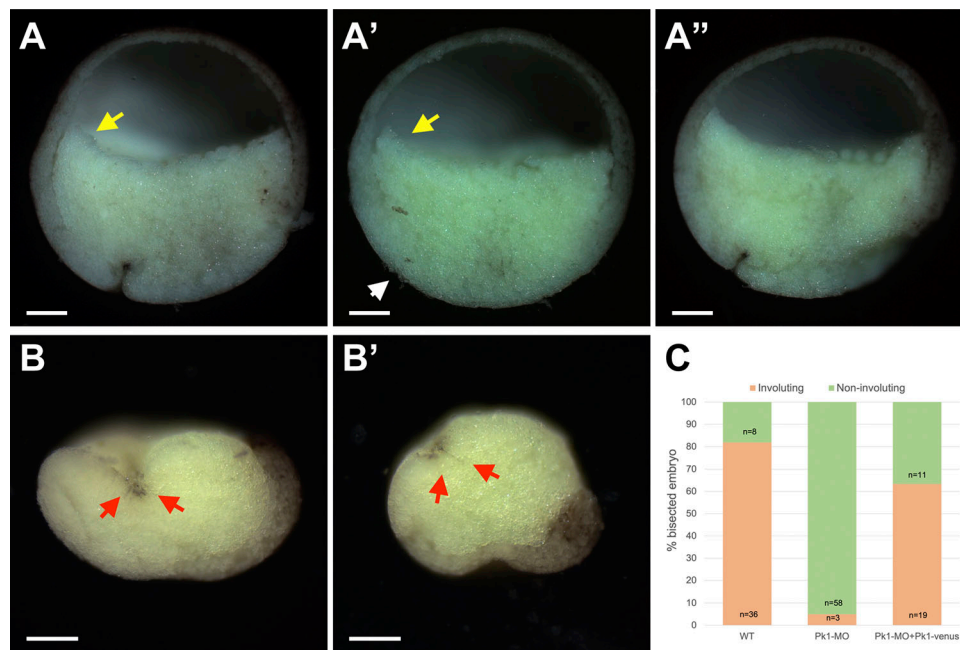


Figure S1. **Gastrulation phenotypes in embryos and lip explants.** (A and A') WT and Pk1-MO embryos at early gastrulation. Scale bars, 100  $\mu$ m. (A'') Gastrulation is rescued by Pk1 mRNA. Scale bar, 100  $\mu$ m. (B and B') Dorsal blastopore lip explants indicated movement defects after Pk1 knockdown. Scale bars, 100  $\mu$ m. (C) Fractions showing involution of WT, Pk1-MO, and rescued embryos. *n*, number of embryos.

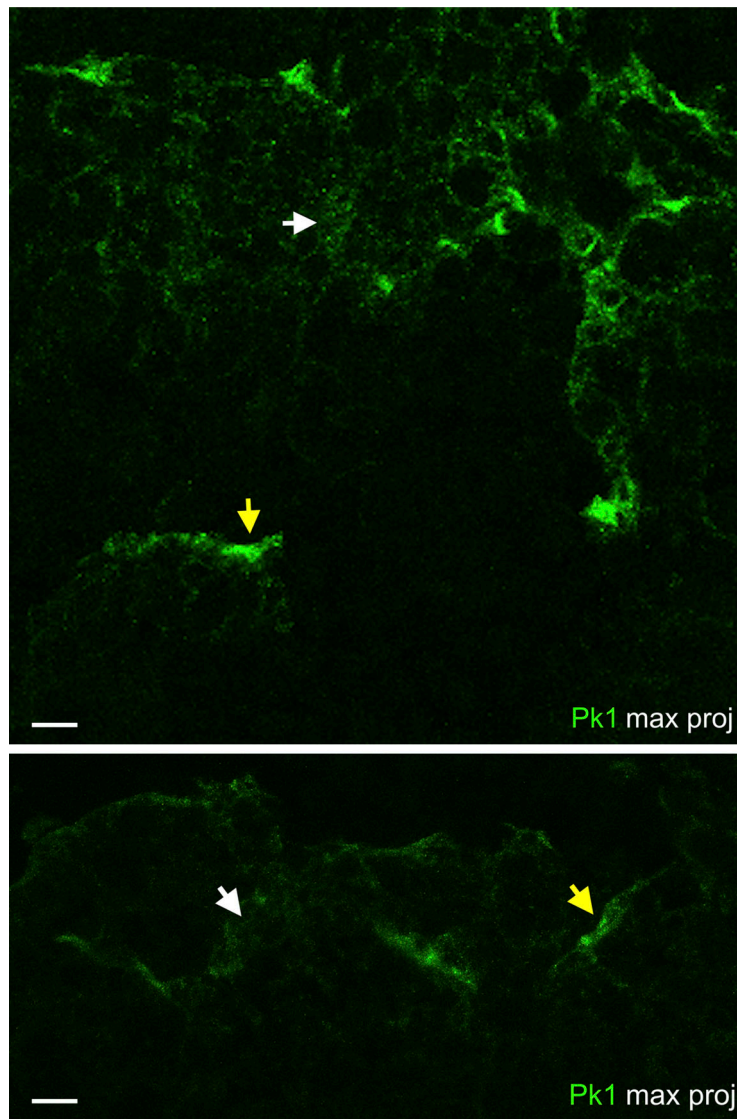


Figure S2. **Endogenous Pk expression in the PCM shown by Pk1 antibody staining.** White arrows, diffuse Pk1; yellow arrows, Pk1 plaques.

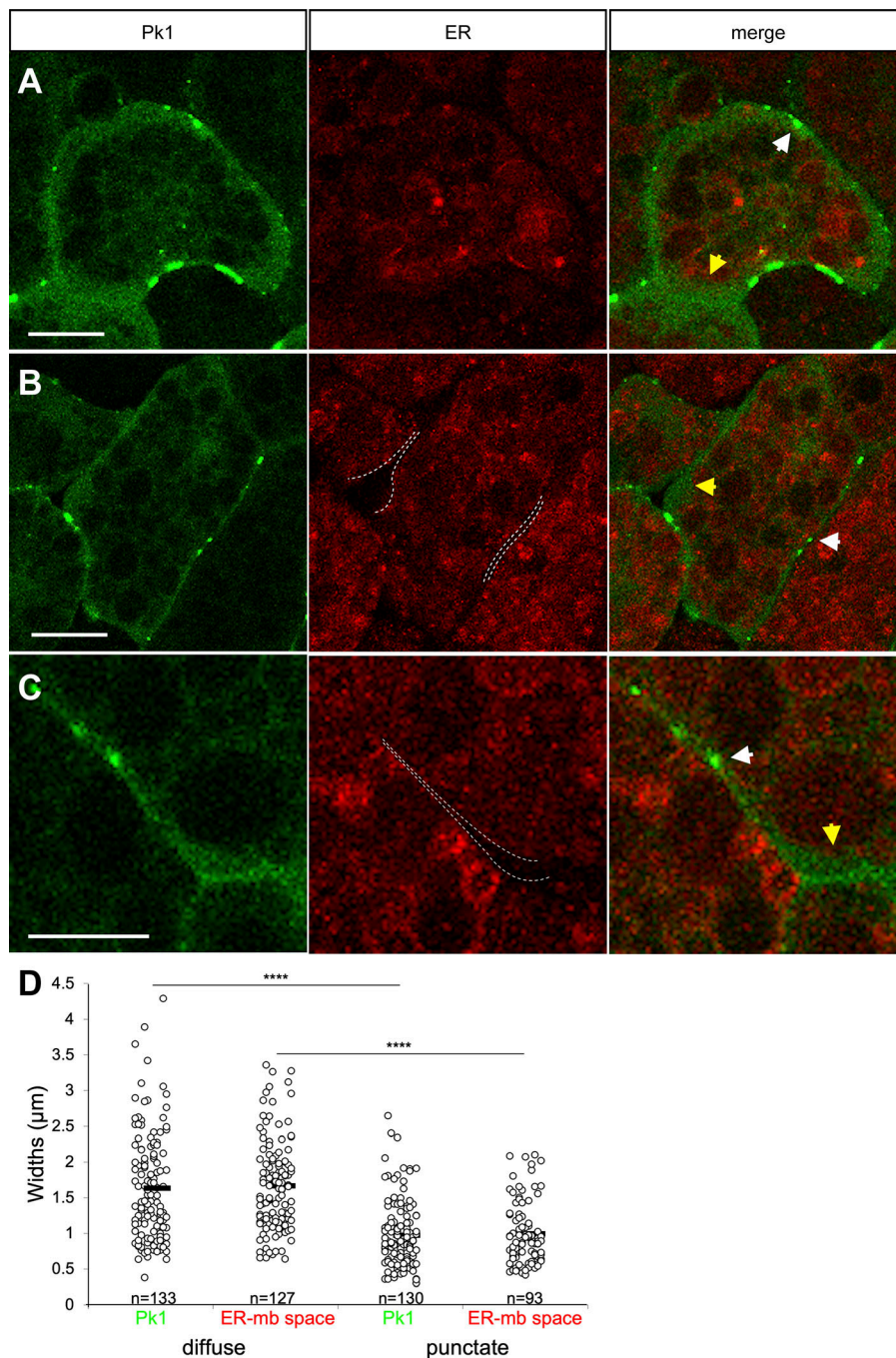


Figure S3. **Pk1 is enriched at the ER-free cell periphery in PCM tissue mosaically labeled with Pk1-venus and ER-Tracker Red. (A–C)** PCM explants labeled with Pk1-venus and ER-Tracker Red. Dashed lines indicate ER domain boundaries. White arrows, Pk1 puncta and plaques; yellow arrows, puncta-less regions of cell periphery. Scale bars, 10  $\mu\text{m}$ . **(D)** Widths of Pk1 zone and ER-membrane space in PCM explants. At diffuse Pk1: Pk1,  $n = 133$ ; ER-membrane space,  $n = 127$ . At puncta: Pk1,  $n = 130$ ; ER-membrane space,  $n = 93$ .  $n$ , number of cells. \*\*\*\*,  $P \leq 0.0001$  in a two-tailed Student's  $t$  test. Data distribution was assumed to be normal but was not formally tested.

Video 1. **Cell migration and radial intercalation in a WT PCM explant.** Light microscopy time-lapse video showing deep cell migration toward the BCR (pigmented cells on right) and exchange of cell neighbors. Cells reaching the tissue boundary radially intercalated to contact the BCR. Time is shown in minutes. Frame rate: 25 frames/second.

Video 2. **Cell movements in a Pk1 morphant PCM explant.** Light microscopy time-lapse video showing attenuated cell migration velocity and radial intercalation after Pk1 knockdown with 40 pg Pk1-MO. Cells remained attached to neighbors and were stretched toward the boundary (on right). Time is shown in minutes. Frame rate: 25 frames/second.

Video 3. **Bleb formation and retraction in a nonattached PCM cell.** Confocal microscopy time-lapse video showing the formation and retraction of a bleb as the membrane detached locally from the cortex and as F-actin reassembled at the detached membrane, respectively. Green, LifeAct-GFP. Time is shown in minutes. Frame rate: 25 frames/second.

Video 4. **Bleb collapsed after TBB treatment in a PCM cell.** Confocal microscopy time-lapse video showing diminished F-actin reassembly at the detached membrane shortly after 10  $\mu$ M TBB was added and collapse of the blebs onto the cell surface. Green, LifeAct-GFP. Time is shown in minutes. Frame rate: 25 frames/second.

Video 5. **Cell tail retraction in Pk1 morphant PCM tissue.** Confocal microscopy time-lapse video showing the formation of a F-actin-filled retraction fiber at the cell tail in a Pk1 morphant PCM explant (40 pg Pk1-MO). During tail retraction, F-actin separated from the membrane tube and recoiled, and the membrane was left behind as a tether. Red, mbRFP; green, LifeAct-GFP. Time is shown in minutes. Frame rate: 25 frames/second.

Video 6. **Dynamics of Pk1 puncta at separating PCM cell contacts.** Confocal microscopy time-lapse video showing the formation and association of puncta with the periphery of cell contacts as the membranes separate. Red, mbRFP; green, Pk1-venus. Time is shown in minutes. Frame rate: 25 frames/second.